Colloquium: Nanoplasmas generated by intense radiation

Kostya (Ken) Ostrikov*

School of Chemistry, Physics, and Mechanical Engineering, Queensland University of Technology (QUT), Brisbane QLD 4000, Australia and Commonwealth Scientific and Industrial Research Organisation, P.O. Box 218, Lindfield NSW 2070, Australia

Farhat Beg

High-Energy-Density Physics Group, Centre for Energy Research, University of California San Diego, California 92093, USA

Andrew Ng

Atomic, Molecular, and Optical Physics Group, University of British Columbia, Vancouver, British Columbia, V6T 1Z1, Canada

(published 25 January 2016)

Solid, liquid, and gaseous states of matter can exist and acquire unique properties when reduced in size into a nanometer domain. This Colloquium explores the approaches to produce plasmas with nanometer dimensions and the arising physical phenomena and properties associated with this extreme, nonequilibrium state of matter. Analysis of the spatial confinement, coupling, ideality, and degeneracy criteria lead to the possibilities to produce transient nanoplasma states *near*, *in*, and *from* solids by using ultrafast photoexcitation. These states arise through the interplay of nonequilibrium, many-body Coulomb interactions, thermal, and nonthermal effects. Examples include photoexcited electron-hole plasmas in semiconductors, transient solid-to-plasma states including warm dense matter, nanoplasmas produced by interaction of nanoclusters and nanoparticles with intense radiation, nanoplasmas in high-energy ion tracks within solids, nanoplasmas in relativistic regime, and others. Physical phenomena arising due to the localization of high-energy densities to microscales and nanoscales and their potential applications are discussed.

DOI: 10.1103/RevModPhys.88.011001

CONTENTS

I. INTRODUCTION

It is well known that the sizes of solid, liquid, and gaseous matter can be reduced to nanoscales. This size reduction leads to many unusual properties and behaviors that are not common to the corresponding bulk states (Barth, Costantini, and Kern, 2005; Bader, 2006; Charlier, Blase, and Roche, 2007; Wang *et al.*, 2007; Castro Neto *et al.*, 2009). This causes one to question what will happen if the size of the fourth, most extreme, plasma state of matter is also reduced to the nanoscale, how can one produce nanoplasmas, and what unusual properties can be achieved?

This Colloquium explores the various options to produce nanoplasmas and the arising challenges in the generation and stability of this highly unusual state of matter, which is not as common as nanoscale solids, liquids, and gases. In the following, we define nanoplasmas, introduce common situations when they may be generated, and discuss the

*Also with School of Physics, The University of Sydney, Sydney NSW 2006, Australia.
kostya.ostrikov@qut.edu.au
kostya.ostrikov@csiro.au

associated technical challenges and concept limitations upon size reduction.

II. PLASMA CRITERIA AND NANOPLASMAS

According to the classical definition, plasma is a fully or partially ionized, overall charge neutral, electrically conducting (typically gaseous) medium which exhibits collective behavior of charged species which is governed by Coulomb interactions (Chen, 1984). The specific type of plasmas is determined by the energy and interactions of the species involved and is characterized by spatial confinement, coupling, ideality, and degeneracy. The concept of *nanoplasma* may be defined similarly to nanoscale solid matter, namely, by limiting at least one dimension of the plasma to the nanometer range. A more precise definition and the associated limitations will follow.

In terms of spatial confinement, nanoplasma states may most likely be produced *in*, *near*, or *from* solids. The first case refers to situations when matter shows plasmalike behavior and properties when confined within solids with at least one dimension in the nanometer range (e.g., smaller than a few hundred nm). The second case holds when nanoplasmas are produced near solids, e.g., in microchannels or voids or near nanoclusters or nanoparticles. The last situation may happen when originally solid nanomatter becomes ionized upon evaporation or explosion thus forming nanoplasmas.

Association of nanoplasmas with solids is not accidental. Indeed, a large number of charged species (and, hence, number densities) is required to exhibit collective plasmalike behavior, even upon size reduction to the nanoscales. In this case it is also difficult to establish and retain the screened Coulomb interactions that are most common for gaseous plasmas.

The spatial scale of the charge separation and screening λ_S is determined by the long-range Coulomb interactions which lead to collective motions of the charged particles (such as plasma oscillations). These oscillations are fundamentally different from collective motions in nonionized (neutral) gases that arise due to short-range interparticle collisions. Persistence of the long-range interactions is one of the reasons why it is so difficult to reduce the plasma sizes to nanoscales.

Solids are suitable to provide sufficiently high densities of charged carriers to generate nanoplasmas. Nanosized solids or their features also serve as "nanocontainers" when nanoplasmas are generated in solids, "rigid boundaries" when nanoplasmas are generated near solids, and as a dense source material in the case when nanoplasmas are produced from solids.

This leads to the definition of nanoplasmas as an ionized, overall charge neutral, electrically conducting medium which shows screened Coulomb interactions and collective behavior of charged species when contained within nanometer-range solid objects (in solids) or extends not farther than a few hundred nanometers beyond the boundaries (near solids) or the original source material (from solids).

Interestingly, free electrons exhibit plasmalike (plasmon) oscillations around lattice ions in nanometer-sized metal nanoparticles. This overall charge neutral medium formally satisfies the previous definition (Pines, 1956; Zayats, Smolyaninov, and Maradudin, 2005; Willets and van Duyne, 2007). However, relatively weak coupling between the constituent species is what differs plasmas from solids.

The degree of coupling between the plasma species j is determined by the relative values of the potential energy of Coulomb interactions $Z_j^2 n_j^{1/3}/\varepsilon_m$ and the thermal energy $k_B T_j$, where ε_m is the dielectric constant of the medium, Z_j, n_j, and T_j are the electric charge (expressed in elementary electron charges e), number densities, and thermal energy of the species j, respectively, and k_B is the Boltzmann's constant.

The coupling parameter

$$\Gamma_j = Z_j^2 n_j^{1/3}/\varepsilon_m k_B T_j \tag{1}$$

is $\Gamma_j^{\text{wc-pl}} \ll 1$ for weakly coupled plasmas while the opposite inequality $\Gamma_j^{\text{sc-pl}} \gg 1$ holds for strongly coupled plasmas (Morfill and Ivlev, 2009). An example of the localized states with the attributes of strongly coupled plasmas is the warm dense matter (WDM) produced in nanometer-thin metal foils (Sec. VI.B).

In several examples presented in this Colloquium, nanoplasmas are nonideal, in other words sufficiently dense so that the effects of interparticle interactions appear to be substantial (Fortov and Iakubov, 2000). In ideal plasmas, the number N_D of charged species within the Debye sphere should be large ($N_D \gg 1$). The radius of this sphere is the electron Debye length

$$\lambda_{De} = (k_B T_e/4\pi n_e e^2)^{1/2} \propto T_e^{1/2} n_e^{-1/2}, \tag{2}$$

which defines the spatial scale of charge separation and consequently, the minimum spatial localization scale of the plasma. Hence,

$$N_D = (4/3)\lambda_{De}^3 n_e \propto T_e^{3/2} n_e^{-1/2}, \tag{3}$$

where n_e is the electron number density (or the ion density n_i due to the overall charge neutrality) and T_e is the electron temperature.

The fundamental limitation is that when the inequality $N_D \gg 1$ does not hold, the concept of the Debye screening is no longer applicable. A more generic concept of the electrostatic screening length λ_S (Dobrynin, Colby, and Rubinstein, 1995) should be used instead of λ_{De} when $N_D \leq 1$.

The Debye length (2) determines the smallest scale of collective motions to develop due to the screened Coulomb interactions. When the Debye length concept is not valid ($N_D \leq 1$), the fundamental length scales to ensure collective particle interactions are determined by the interatomic distance $d \sim n_i^{-1/3}$ (which is a lattice constant in solids) and the electron de Broglie wavelength $\lambda_{dB} = h/p$, where p is the electron momentum and h is the Planck constant.

One may notice that both λ_{De} and N_D scale similarly with the electron density $\propto n_e^{-1/2}$ but quite differently with the electron temperature, namely, $\propto T_e^{1/2}$ and $\propto T_e^{3/2}$, respectively. In other words, achieving proper Debye screening at the nanoscale is very challenging because as the density increases, both λ_{De} and N_D decrease with the same rate. Consequently, at fixed T_e, the inequality $N_D \gg 1$ may hold for lower densities and become invalid at higher densities when λ_{De} reaches the nanometer domain. However, as N_D increases faster with T_e, increasing the electron temperature may be an effective means to achieve the required large number of electric charges within the Debye

sphere of the pursued small size. For example, when $T_e \sim 3$ keV (as is the case for Coulomb explosion of nanoclusters by intense femtosecond laser radiation discussed in Sec. VII), $N_D \sim 280$ even at the electron density assumed to be of the same order of magnitude as the density of the clusters in the solid state ($n_e \sim 10^{23}$ cm^{-3}). In this case, the estimate for the Debye length λ_{De} is ~1.3 nm. This estimate shows that at such high densities the number of particles in nanometer-sized volumes may be large and the effects of interparticle interactions, i.e., nonideality, are important. Nonetheless, since the thermal energy is very high, it is also possible that the plasma may be ideal, provided that the energy of interparticle interactions is small compared to the thermal energy.

At lower energies and similarly high densities, the plasma may become degenerate. In this case, the size reduction may be possible if higher-energy quantum states for electrons are available. According to the Pauli exclusion principle, the individual electrons must have unique quantum states. This is likely to happen when the electron thermal energy $k_B T_e$ is comparable with the Fermi energy E_F and quantum effects are therefore important.

The plasma degeneracy parameter $\Theta = n_e \lambda_{dB}^3$ shows the number of electrons in the elementary volume with a linear size equal to the thermal de Broglie wavelength λ_{dB} (Fortov and Iakubov, 2000) and scales with the electron density and temperature as $\Theta \propto n_e T_e^{-3/2}$. The criterion for degeneracy is $\Theta \gg 1$; hence degenerate plasma states are more likely to appear at high densities and low temperatures.

III. REDUCING PLASMAS TO NANOSCALES: APPROACH AND OPTIONS CONSIDERED

As discussed in Sec. II, collective motions is one of the key attributes of the plasma state. Plasma oscillations that arise due to the restoring electric force upon even a small separation of positive and negative charges with respect to each other is perhaps the most common manifestation of the collective responses of the plasmas. The eigenfrequency of these oscillations, the plasma frequency, is

$$\omega_p = (4\pi n_e e^2/m_e)^{1/2}, \tag{4}$$

where m_e is the electron mass. Similar plasma oscillations arise under resonant conditions in solids (e.g., free-electron metals) and the associated quanta of these oscillations are commonly termed plasmons (Pines, 1956).

These oscillations should continue to persist and ideally be measurable upon the generation of the nanoplasma states. The latter states should feature weaker coupling between the constituent species compared to unperturbed solids and have attributes of weakly or strongly coupled plasmas. To achieve nanoplasma states *in solids*, one should produce equal numbers of negatively and positively charged species within the solid.

The most common way to generate plasmas is by using ionizing radiation which first excites electrons. The typical times required for the excited electrons to exchange the energy with other electrons (electron-electron relaxation time) and ions (electron-ion relaxation time) in solids are $\tau_{ee} \sim 10^{-14}$ s and $\tau_{ei} \sim 10^{-12}$ s, respectively (Silvestrelli *et al.*, 1996).

The effectiveness of ionization is determined by the amount of energy absorbed by the solid, expressed, e.g., in J/g or eV/atom. This energy is determined by the intensity of radiation (irradiance) $I_{\rm rad} = W_{\rm del}/\tau_{\rm del}$ (W/cm^2) and can be delivered differently depending on the energy density delivered per unit surface $W_{\rm del}$ (fluence, J/cm^2), and the duration of the energy delivery pulse $\tau_{\rm del}$ (s). Consequently, the magnitude of $I_{\rm rad}$ and the relative values of $\tau_{\rm del}$, τ_{ee}, and τ_{ei} determine the effect of the radiation on the solid. Increasing $I_{\rm rad}$ is a way to increase the ionization efficiency and hence, to generate sufficiently dense and hot plasmas with the aim to satisfy $N_D \gg 1$.

At sufficiently high $I_{\rm rad}$, if $\tau_{\rm del} \gg \tau_{ei}$ the energy transfer from the electrons to the lattice ions is effective and the solid may melt or even evaporate. However, when $\tau_{ee} \leq \tau_{\rm del} \ll \tau_{ei}$, the energy transfer from the electrons to the ions is not effective and the solid may remain stable as a whole even at very high radiation intensities. This inequality is satisfied for $\tau_{\rm del} \sim 10$–100 fs (1 fs $= 10^{-15}$ s), which is a typical pulse duration of the present-day pulsed femtosecond lasers.

Therefore, using intense radiation with the duration in the femtosecond range may indeed be a viable strategy to generate nanoplasmas in solids below a threshold of radiation intensity $I_{\rm rad}^{\rm abl}$ when the solid is partially or fully ablated. If this threshold is exceeded and other conditions (e.g., localization) are met, nanoplasmas near or from solids may be generated. On the other hand, established experimental techniques to detect and guide fs-laser radiation make it feasible to detect the "signature" attribute of the plasma state—collective plasma oscillations.

Among a few possible options, these considerations determine our focus on nanoplasma generation using sufficiently dense solid matter as a starting material and, in most cases, femtosecond lasers as the excitation source. This type of irradiation makes it possible to produce strongly nonequilibrium electron-hole and electron-ion systems within solids without any significant thermal disassembly (melting) of solid lattices, below certain absorbed energy densities. As considered in Sec. VI.A, this is one of the possibilities to enable athermal lattice disassembly, a critical factor on the way to produce localized nanoplasma states.

Specifically, here we consider the following cases of photoexcited plasmalike states (Fig. 1):

- Electron-hole photoexcited plasmas of semiconductors [Fig. 1(a)]. These plasmas are produced at low temperatures and typical radiation intensities ~10^7–10^8 W/cm^2.
- Photoexcited plasmas in solids by athermal lattice disassembly and generation of WDM as intermediate states [Fig. 1(b)]. Typical laser intensities that produce these effects in semiconductors and metals are ~10^{13}–10^{17} W/cm^2.
- Nanoplasmas produced by interaction of nanoclusters and small nanoparticles with intense laser fields of $I_{\rm rad} \sim 10^{14}$–10^{17} W/cm^2 [Fig. 1(c)].
- Nanoplasmas under subrelativistic and relativistic conditions of high-intensity ($> 10^{18}$ W/cm^2) photoexcitation in semiconducting and metallic nanostructures [Fig. 1(d)] and their applications for generation of ultrahigh currents and magnetic fields.

We also discuss possible nanoplasma-related effects in solids within high-energy ion tracks [Fig. 1(e)] and

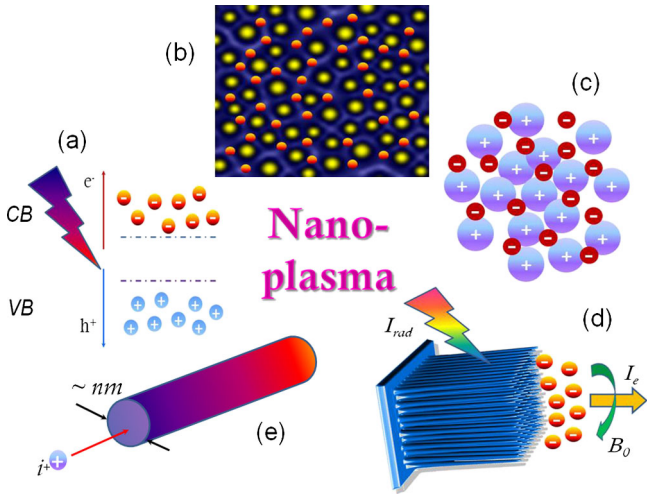

FIG. 1. Examples of nanoplasma-related physical systems: (a) plasmas of photoexcited electrons and holes in semiconductors (Sec. V), (b) transient states from solids to plasmas such as warm dense matter (Sec. VI), (c) nanoplasmas from irradiated clusters and nanoparticles (Sec. VII), (d) photoexcitation of nanostructures to generate hot electrons and strong magnetic fields (Sec. IX), and (e) ion tracks generated by energetic ion projectiles in solids (Sec. VIII).

nanoplasmas near solids confined to hollow waveguides. In these cases, we focus on the spatial localization of the possible nanoplasma states and discuss the most important physical (e.g., energy transfer and relaxation, charge coupling, degeneracy, collective motions, etc.) processes. We also discuss possible or potential size-dependent effects, which are among the most important features studied in nanoscale science. One of the aims of this Colloquium is to show how the plasmalike excitation phenomena vary with the intensity of radiation. In most cases the phenomena considered are arranged in order of increasing I_{rad}.

One of the most common manifestations of size-dependent effects is through the dependence of characteristic temporal and spatial scales of plasmalike collective motions on the number of particles, object size, and geometry. Starting from very low radiation intensities, plasmalike collective excitations (plasmons) can be excited in metal nanoparticles under resonant conditions, yet without nanoplasma generation or even partial lattice disassembly. These effects are discussed in the following section mostly because of the size-, geometry-, and electron-density-dependent effects that are clearly resolved at nanoscales. Quite similar plasmonic effects are highly promising to establish and quantify the collective behavior of nanoplasma states produced at much higher radiation intensities. This discussion is also included because the plasmons (quanta of the plasmalike electron excitations) in nanoparticles are often confused with nanoplasmas.

IV. NANOPLASMA EFFECTS IN SOLIDS WITHOUT PLASMA GENERATION

Here we consider localized surface plasmons in metal nanoparticles where a fast response of free-electron gas under *resonant excitation* conditions shows clear plasmalike responses—plasmons (Pines, 1956; Maier and Atwater, 2005; Zayats, Smolyaninov, and Maradudin, 2005; Stockman, 2011; Wang, Plummer, and Kempa, 2011). Well-established production of common plasmonic nanoparticles with a relatively low optical loss (e.g., Ag, Au, etc.), excitation of plasmons using low-intensity, noncoherent sources of (e.g., white) light, and optical detection of plasmonic resonances makes low-radiation-intensity plasmonics an ideal test bed for the studies of size-, shape-, and density-dependent properties at nanoscales. These properties arise from electron collective responses within metal nanoparticles and make it possible to confine and control light at subwavelength scales. This ability may potentially be extended to much higher radiation intensities when nanoplasmas are generated; see Sec. VI.C.

Importantly, even though the photoexcited resonant collective oscillations of electron gas appear at the plasma frequency (eigenfrequency of the plasmon resonance) $\omega = \omega_p$, the energy absorbed by the nanoparticles in typical room-temperature, low-radiation-intensity plasmonic experiments is very low, and the nanoparticles remain in the solid state. In this case, the nanoplasmalike responses arise from collective motions of the free-electron gas confined to the nanometer dimensions whereas the coupling between the positively charged lattice ions remains the same as in the unperturbed solid state. Because the electron densities in metals are very high $n_e \sim 10^{23}$ cm^{-3}, the electron gas is degenerate ($\Theta \gg 1$) even at room-temperature conditions.

A. Nanoplasma effects in free-electron nanosolids

Characteristic plasma oscillations (plasmons) (Pines, 1956; Stockman, 2011) are typical in plasmonic nanostructures and depend on the properties (e.g., density and degree of collisional losses) of charge carriers as well as the nanoparticle size and shape (Fig. 2). These excitations owe their existence to collective responses of the gas of free electrons that oscillate around a stationary positively charged background made of lattice ions, similar to plasmas in gases. The electromagnetic energy is confined to nanometer dimensions. In the case of localized surface plasmons (LSPs) excited in metal nanoparticles (NPs), this confinement is three dimensional. Nanoscale energy localization of these collective plasmalike excitations enables many interesting plasmonic effects such as light energy confinement to nanoscale dimensions that are much smaller than the wavelength of visible and even UV light (Wang, Plummer, and Kempa, 2011).

When the free-electron gas is displaced with respect to the neutralizing background of the lattice ions, the restoring electric force leads to the plasma oscillations at the frequency of the LSP resonance, which is determined by the number density of free electrons in the metal as well as the NP size and geometry [Fig. 2(a)] (Stockman, Faleev, and Bergman, 2001). For silver, the plasma frequency is $\omega_p \sim 1.2 \times 10^{16}$ s^{-1}. To excite the plasma oscillations at such frequency, the external electromagnetic field should typically be in the optical range. At such frequencies, the penetration depth of the optical field in Ag is ~20 nm, where the electrons are effectively displaced.

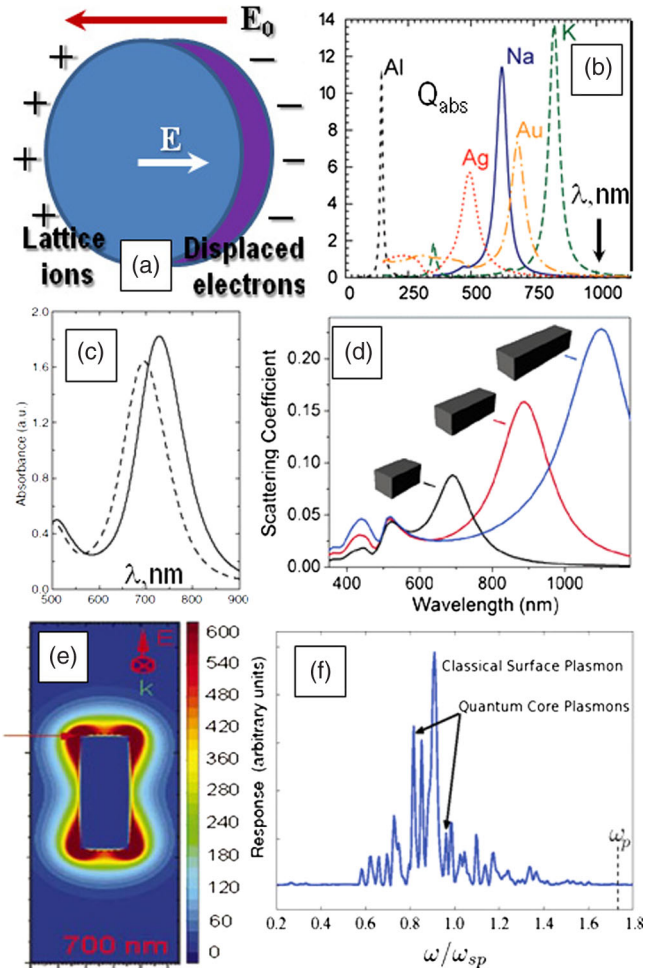

FIG. 2. Nanoplasma effects in plasmonic NPs. (a) LSP excitation in a spherical metal NP in an external electric field E_0. (b) Peaks in optical absorption spectra corresponding to metals with different electron densities. Adapted from Blaber, Arnold, and Ford, 2009. (c) Higher electron density causes a blueshift in the absorbance spectra. Adapted from Mulvaney *et al.*, 2006. (d) Increasing the aspect ratio of rectangular nanorods leads to redshifted resonance peaks. Adapted from Wiley *et al.*, 2007. (e) Enhancement of electromagnetic fields around a silver nanorod polarized along the long axis. Adapted from Hao and Schatz, 2004. The maximum field is near the edges and is shown by an arrow. (f) Quantization of plasmon resonances in a small spherical Au NP. Adapted from Townsend and Bryant, 2012.

The eigenfrequency of the plasmonic resonator (Bliokh *et al.*, 2008) depends on the electron density, which varies from one metal to another. Indeed, the plasmon energies $\hbar\omega_p$ are 3.72, 5.71, 8.55, 9.6, and 15.3 eV for K, Na, Au, Ag, and Al, respectively, where $\hbar$ is the reduced Planck's constant. These values were used to compute the resonant peaks for all these metals in a nanoshell configuration as shown in Fig. 2(b) (Blaber, Arnold, and Ford, 2009). When additional electrons are injected into NPs, the electron density increases, which leads to the higher resonance frequencies and, hence, the blueshift of the resonance peak [Fig. 2(c)] (Mulvaney *et al.*, 2006).

B. Size-dependent plasmon effects

The frequencies of plasmonic resonances depend on the nanoparticle size and shape. Assuming the simple free-electron form $\varepsilon(\omega) = 1 - (\omega_p/\omega)^2$ for the dielectric function of the metallic spherical NP, one has

$$\omega_{\rm res}^{\ell} = \omega_p \sqrt{\ell/[\varepsilon_0(\ell+1)+\ell]}, \tag{5}$$

where ε_0 is a dielectric constant of a bounding medium and ℓ is an integer (Zayats, Smolyaninov, and Maradudin, 2005). For small spheres, only the dipole $\ell = 1$ mode is important. For a sphere bounded with vacuum, the plasmon resonance frequency is $\omega = \omega_p/\sqrt{3}$. For larger spheres, contributions of larger multipoles become more important and in the limit of a very large sphere ($\ell \to \infty$), the frequency (5) approaches the surface plasmon resonance at a planar dielectric-metal interface

$$\omega = \omega_p/\sqrt{\varepsilon_0 + 1}, \tag{6}$$

which is $\omega = \omega_p/\sqrt{2}$ for a metal-vacuum interface.

When the aspect ratio of the nanoparticle changes, the carrier polarization is no longer isotropic. For example, when the NP is elongated in one direction [e.g., a nanorod in Fig. 2(d)], the charge separation takes place in two dimensions, namely, along and across the main axis. This gives rise to the short-axis and long-axis modes with shorter and longer wavelengths, respectively. As the main axis becomes longer, the restoring force in that direction decreases giving rise to the strong redshift of the long-axis modes seen in Fig. 2(d) (Wiley *et al.*, 2007). Under resonant conditions, the electromagnetic field is strongly amplified within the particle and is fairly uniform for small NPs (Maier and Atwater, 2005). The polarization and density of electron states varies among different nanoparticle shapes and affects the resulting plasmonic responses.

A strong dipole field is thus generated outside a nanorod sketched in Fig. 2(e) (Hao and Schatz, 2004). The strong polarization of the carriers leads to very nonuniform distributions of the electron density in different surface areas of the nanorod. This in turn leads to the similarly nonuniform field enhancement around the nanorod, with the strongest effect seen near the sharp edges [Fig. 2(e)].

The spatial localization of this field is comparable to the nanoparticle size, which can be used for the effective scattering and focusing of light. This effect leads to the generation of nanoplasmas (near solids) in a liquid surrounding a gold nanoparticle (Boulais, Lachaine, and Meunier, 2012) and within a hollow waveguide with submicrometer dimensions (Sivis and Ropers, 2013); see Sec. VIII.

As the NP size decreases, surface and quantum effects play a more and more significant role. During one plasmon oscillation with a typical fs duration, an electron moving with a typical Fermi velocity $V_F \sim (1.4\text{–}2.0) \times 10^6$ m/s (lowest and highest values are for Au and Al, respectively) is able to cross a distance up to ~2 nm. When the nanoparticle size is comparable with this characteristic distance (nonlocality length), the surface scattering and electron

delocalization effects come into play. In the billiard model (Blaber, Arnold, and Ford, 2009), the surface scattering leads to the specific damping with the rate $\gamma_{\rm scat} = V_F/\lambda_{\rm mfp}$, where $\lambda_{\rm mfp}$ is the electron's mean free path between two consecutive collisions with the walls.

Within the Drude model (Zayats, Smolyaninov, and Maradudin, 2005), the total damping rate

$$\gamma = \gamma_{\rm intra} + \gamma_{\rm scat}, \tag{7}$$

where $\gamma_{\rm intra}$ is the intraband damping rate, determines the imaginary part ε'' of the complex dielectric permittivity

$$\varepsilon = \varepsilon' + i\varepsilon'', \tag{8}$$

and, hence, the Q factor [which characterizes the level of losses in the system and is determined by the ratio of the resonant frequency to the half-width of the resonant peak in the spectrum (Bliokh *et al.*, 2008)] is

$$Q = |\varepsilon'|/\varepsilon''.$$

In the weak damping case when $\gamma \ll \omega$,

$$\varepsilon' = 1 - \frac{(\omega_p^{\rm eff})^2}{\omega^2}, \tag{9}$$

where $\omega_p^{\rm eff}$ is the effective plasma frequency which may be different from the bulk plasma frequency ω_p, e.g., due to geometrical factors. When the level of losses is low, the plasmalike effects become more important, especially in the vicinity of the plasmon resonance $\varepsilon'(\omega) = -1$. This is why it is particularly important to minimize the losses, which are typically quite high in the optical range.

The effective plasma frequency $\omega_p^{\rm eff}$ can be smaller than ω_p (Silverinha, 2009). This has several important consequences. First, if $\omega_p^{\rm eff}$ can be reduced, the material becomes transparent to lower (e.g., infrared or terahertz) frequencies. In these frequency ranges, the losses are relatively lower, hence, the importance of the plasmalike effects increases. A viable way to reduce $\omega_p^{\rm eff}$ is by designing artificial metamaterials with nanometer features. In this case, the geometric factors and the plasmalike effects interplay constructively to enable unique electromagnetic properties including optical negative index, enhanced transparency, and reduced losses (Shalaev, 2007).

For example, theoretical calculations show that the three-dimensional scaffoldlike structure made of metal nanowires (NWs) mimics the properties of a local isotropic plasma medium and allows operation at infrared frequencies, with substantially reduced losses and spatial dispersion effects that affect the performance of some metamaterials (Silverinha, 2009). In this case, the effective plasma frequency can be obtained from

$$\frac{1}{(\omega_p^{\rm eff})^2} = \frac{1}{\omega_p^2 f_V} + \frac{1}{\beta_p^2 c^2}, \tag{10}$$

where $f_V = \pi R^2/a^2$ is the volume fraction of the nanowires with radius R. The spacing between the nanowires is $a/2$. In Eq. (10),

$$\beta_p = \left[\frac{2\pi/a^2}{\ln(a/2\pi R) + \upsilon_1}\right]^{1/2} \tag{11}$$

is the geometric factor, where $\upsilon_1 = 0.5275$ (Silverinha, 2009).

If the electron density is such that $R \gg \delta_s$, where

$$\delta_s = c/\omega_p \tag{12}$$

is the skin (field penetration) depth, the ratio between the damping and the plasma frequencies of the effective medium (10) may be much smaller compared to the bulk metal, even if f_V is small. In this case, the loss in the effective medium (metamaterial) may be negligible and the medium would operate as isotropic loss-free *artificial* "nanoplasmas" made of perfectly conducting nanowires (Silverinha, 2009). We emphasize that these calculations correspond to low radiation intensities and the generation of nanoplasma states is not possible in this case.

This example suggests that the customized nanoscale design of metamaterials is a viable way to maximize plasma-like effects in nanometer-sized plasmonic structures in the infrared and terahertz frequency ranges, which are of interest in medical imaging, homeland security, telecommunications, and several other applications. Recent advances in precise measurements of electromagnetic waves in nanoelectronic devices using terahertz spectroscopy open new possibilities for both fundamental and applied research in this area (Nouvel *et al.*, 2009).

From the viewpoint of theoretical formalism, incorporation of cold plasma equations into the Fourier modal method is instrumental in the analysis of optical responses (e.g., higher harmonics generation) from metal nanostructures which is consistent with numerous experimental results (Paul, Rockstuhl, and Lederer, 2011). This further supports the relevance of plasmalike effects to functional properties of solid nanostructures. Indeed, plasma phenomena in the solid state lead to interesting effects that are presently explored in several fields. These phenomena combine some features of gaseous plasmas with those of the solid state such as electron band structure, degeneracy, anisotropy, and others (Raimes, 1957; Jonscher, 1964; Hoyaux, 1968).

For small nanoparticles in the quantum limit, size quantization dramatically modifies the LSP spectrum. An optical spectrum of a small (0.74 nm radius, a single 100 electron Au-jellium sphere model) Au NP computed using time-dependent density functional theory is shown in Fig. 2(f) (Townsend and Bryant, 2012). The spectrum consists of several quantized peaks, with the largest peak redshifted to $0.91\omega_{sp}$, where $\omega_{sp} = \omega_p\sqrt{3}$ is the frequency of plasmon resonance of a metal sphere surrounded by vacuum (5).

This effect is attributed to charge density tunneling outside the nanoparticle, which reduces the restoring force and, hence, slows the plasmon oscillation. This main resonance is due to the electron response over the entire NP and is termed "classical surface plasmon." The "quantum core plasmons" are due to the responses of the electron density near the nanoparticle center and appear only in the quantum treatment. The quantum theory also predicts that the responses of the classical surface plasmons become much larger compared to

the quantum core plasmons as the NP size increases (Townsend and Bryant, 2012).

On the other hand, when temperature is decreased, the de Broglie wavelength of electrons λ_{dB}, which quantifies the extension of electron's wave function due to the quantum uncertainty principle, increases. This is why at lower temperatures, quantum plasmonic effects are expected to be more important and may contribute to the formation of exotic quantum structures such as multishelled quantum droplets in photoexcited semiconductor quantum wells discussed in Sec. V.B. Quantization of plasmon resonance frequencies is consistent with the results (Wang, Plummer, and Kempa, 2011) obtained by using the Feibelman d-function formalism (Feibelman, 1982). These results suggest that LSP resonances can be regarded as standing surface plasmon waves on the nanoparticle circumference $2\pi R$ with the quantized wavelengths $\lambda_{\mathrm{LSP}n} = 2\pi R/n$ depending on the NP radius R, where $n = 1, 2, 3, \ldots$.

The previous discussion is relevant to the collective responses of electron-hole plasmas considered next and other relevant situations considered later in this Colloquium.

V. NANOPLASMAS IN ELECTRON-HOLE SOLIDS

Electron-hole plasmas can be produced in semiconductors either by doping or by photoexcitation across the band gap (Wang, Plummer, and Kempa, 2011). By varying the intensity of the laser beam, the density of charge carriers can be varied. This is quite similar to controlling the density and dissociation degree of gaseous plasmas by varying the discharge power. These carriers can be confined to nanoscales, e.g., in quantum wells and heterostructures, where exotic quantum structures can form.

A. Nonequilibrium dynamics and collective responses

As weak coupling is one of the most common attributes of plasmas and common semiconductors have quite large dielectric constants ($\varepsilon_m \sim 10$) the condition $\Gamma = e^2 n_e^{1/3}/\varepsilon_m k_B T_e \ll 1$ can be satisfied at temperatures ~100 K at carrier densities of the order of $\sim 10^{18}$ cm^{-3} (Keldysh, 1986). Under such conditions, nanoplasmas may be generated provided that the mutually neutralizing gases of electrons and positively charged holes are generated, and the resulting plasmas are contained within nanometer dimensions, e.g., by quantum wells.

However, achieving high plasma densities is quite challenging under thermodynamic equilibrium conditions at such low temperatures, because the carrier density

$$n_e \sim (m_e k_B T_e/\hbar^2)^{3/2} \exp(-\epsilon_g/2k_B T_e) \tag{13}$$

decreases much faster with T_e than the temperature itself, where ϵ_g is the energy band gap, or the minimum energy to produce an electron (e)-hole (h) pair (Keldysh, 1986).

Hence, the carriers should be generated under *nonequilibrium conditions*, for example, by carrier injection or photoexcitation with the energies exceeding ϵ_g. The presence of the band gap in semiconductors (which is absent in free-electron metals) makes it possible to promote electrons from the valence band (VB) to the conducting band (CB) thereby generating equal amounts of neutralizing holes, which creates e-h plasmas (Jeffries, 1975). The density of the plasma can be increased by delivering more and more photons with the energy above the band gap. Such plasmas are commonly produced in semiconducting objects with at least one nanoscale dimension such as nanostructures, heterostructures, and superlattices. Quantum wells formed near interfaces between thin semiconducting layers of nanometer thickness represent ideal nanoscale confinement structures for the plasmas.

Therefore, nonequilibrium photoionization can be used to control the plasma density, and, consequently, the effectiveness of Coulomb screening and the frequency of the arising collective responses from the plasma. In this way, one potentially may produce any high density of electrons. As the intensity of radiation increases, one could hypothetically not only transfer all the electrons from the valence to the conducting band but also remove electrons from the inner shells of atoms and achieve plasmas with ions of a high positive electric charge Z. This happens under certain conditions when nanoplasmas are generated from nanoclusters or small nanoparticles exposed to intense radiation considered in Sec. VII.

The dynamics of electrons and holes is strongly nonequilibrium and involves several stages over distinctive temporal scales. Their collective behavior is characterized by the emergence of the screened Coulomb interactions and plasma oscillations.

Photoexcited electrons and holes first behave like isolated charges and interact by the bare Coulomb potential. The screened Coulomb interaction potential

$$W(\omega, t_D) = \phi_0/\epsilon(\omega, t_D) \tag{14}$$

evolves as the screening cloud forms around the charged carriers which start exhibiting collective behavior (Huber *et al.*, 2001); see Fig. 3. Here ϕ_0 is the bare Coulomb potential of interaction of two isolated point charges, ω is

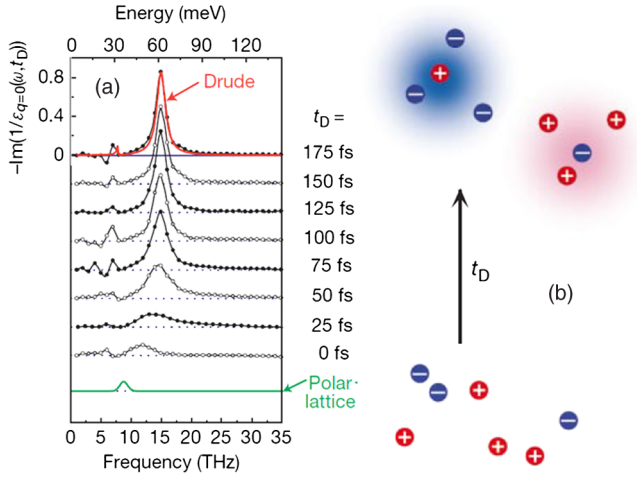

FIG. 3. Temporal dynamics of transition from isolated point charges to electron-hole plasmas. (a) Imaginary part of the inverse dielectric function of GaAs and data fit using the Drude model showing the emergence of the plasma resonance at $\omega_p/2\pi =$ 14.4 THz (60 meV); (b) transition from isolated to correlated and screened charge states. Adapted from Huber *et al.*, 2001.

the excitation frequency, $\epsilon(\omega, t_D)$ is the dielectric function, and t_D is the delay time between the excitation (pump) and the probe signals.

Collective behavior in the many-body nonequilibrium *e-h* system is established over 100 fs scales when the *e-h* plasma in GaAs is generated (Huber *et al.*, 2001). Importantly, the buildup of Coulomb and plasmon scattering of the probe signal passing through a 200-nm-thick epitaxial layer of GaAs on diamond is delayed by t_D of the order of several 10^{-14} s. This delay is comparable to the inverse plasma frequency $\omega_p/2\pi =$ 14.4 THz which appears as a sharp resonance in the inverse imaginary part of the dielectric function of GaAs in Fig. 3(a). The carrier dynamics becomes dominated by scattering with plasmons. The transition to a collective plasma response manifests reorganization of the many-body electron-hole system to the correlated and screened state as sketched in Fig. 3(b).

Note that the energy quanta associated with the plasma oscillation in this case is $\hbar\omega_p = 60$ meV, and the density of photoinduced carriers is $n_e \sim 2 \times 10^{18}$ cm^{-3} (Huber *et al.*, 2001). Under such conditions, the electron-hole plasma is weakly coupled but degenerate and nonideal ($N_D < 1$).

B. Plasma versus exciton states

Coupling of electrons and holes leads to the formation of Wannier-Mott excitons which coexist with the ionized and correlated plasma state in the two-phase region shown in Fig. 4(a). As the temperature increases, the exciton phase becomes dominant, while the electron-hole plasma state prevails at higher densities ($n_e > 5 \times 10^{18}$ cm^{-3}) (Suzuki and Shimano, 2009).

The excitons and electron-hole plasmas may coexist over several hundred picoseconds as demonstrated by ultrafast THz probing of the dynamics of photoexcited quasiparticles quantum confined within a stack of 14-nm-thick GaAs nanolayers separated with 10-nm-thick $Al_{0.3}Ga_{0.7}As$ barriers [lower inset in Fig. 4(b)] (Kaindl *et al.*, 2003). The formation of bound exciton states results in the transition of the induced dielectric function response from the negative (plasmalike) to the positive (dielectriclike) after ~300 ps when the exciton-dominated state is formed [Fig. 4(b)].

This transition may also be interpreted as the transition from the highly ionized electron-hole plasma state to the charge neutral exciton state. Indeed, as the density $n_{e\text{-}h}$ of photoexcited carriers decreases due to the *e-h* recombination and exciton formation, the real part of the complex dielectric function of the fs-laser-irradiated semiconductor (Hillyard, Reis, and Gaffney, 2008)

$$\epsilon_{\mathrm{mod}} = \epsilon_{\mathrm{nex}} - \frac{n_{e\text{-}h}e^2}{\epsilon_0 m^*_{\mathrm{opt}} m_e \omega^2} \frac{1}{1 + i(\omega\tau_D)^{-1}} \qquad (15)$$

shifts to the positive value range. Here ϵ_{nex} is the dielectric constant in the absence of photoexcitation, e.g., $\epsilon_{\mathrm{nex}} = 19.105 + i5.683$ at 1.5 eV for InSb, e is the electron charge, ϵ_0 is the permittivity of free space, ω is the frequency of light used in the photoexcitation process, m^*_{opt} is the optical effective mass of the carriers, and τ_D is the Drude damping time (~1 fs).

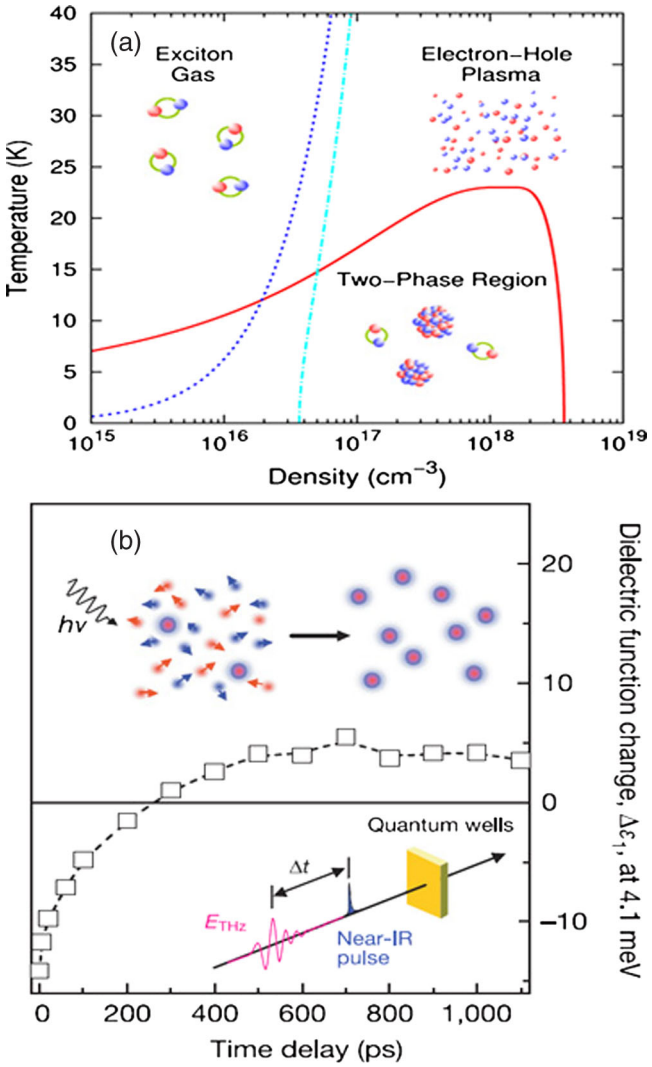

FIG. 4. (a) Phase diagram of the electron-hole system in Si. Adapted from Suzuki and Shimano, 2009. (b) Temporal dynamics of exciton formation from unbound *e-h* gas. The dielectric function changes from negative (conducting, *e-h* plasma state) to positive (dielectric, exciton-dominated state). The inset shows the experimental scheme. Adapted from Kaindl *et al.*, 2003.

The specific many-body configurations of these electron-hole systems are extracted from quantitatively measured time-resolved nonlinear absorption spectra of resonantly excited quantum wells. The microscopic theory assigns the observed spectral changes to a unique mixture of electron-hole plasma, exciton, and polarization effects (Smith *et al.*, 2010). Electron-hole plasmas and bound excitons represent distinctive and correlated subsystems. The host crystal lattice provides a spatially uniform background, which determines the energy spectrum of carriers (effective masses) and their Coulomb interactions (dielectric constant) (Keldysh, 1986).

Photoexcitation of GaAs superlattices may lead to more complex quasiparticles such as biexcitons and quantum droplets (dropletons) sketched in Fig. 5(a) (Almand-Hunter *et al.*, 2014). These states are characterized with different binding energies E_{bind} between quasiparticles. The mixture of the particles can be controlled by the number of photons in the

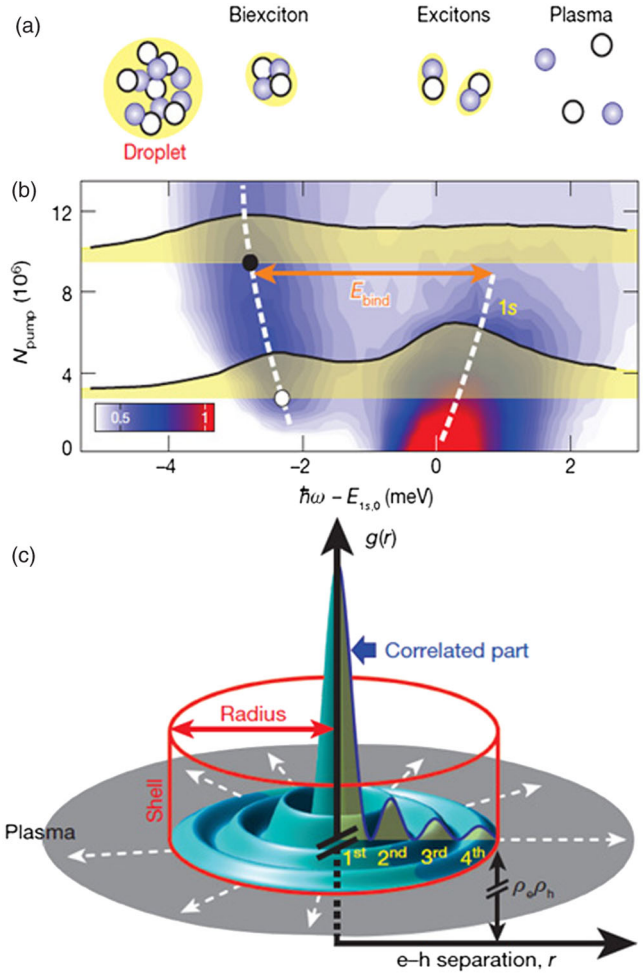

FIG. 5. Quasiparticles in direct-gap semiconductors with two types of charge carriers (electrons and holes). (a) The interplay between the nonequilibria, many-body interactions and thermalization effects determines the specific quantum state. (b) Binding energy of *e-h* states for a different number of photons in the excitation pulse and the difference between the photon energy and the low-density exciton energy. (c) Computed *e-h* pair correlation function $g(r)$ for a quantum droplet with the radius $R = 91$ nm. The cylinder represents the droplet shell while the dark area corresponds to the plasma. Adapted from Almand-Hunter *et al.*, 2014.

pump pulse N_{pump} [Fig. 5(b)]. At higher N_{pump}, the state of the system deviates significantly from the low-density exciton states [sketched on the upper left in Fig. 4(a)] with the energy $E_{1s,0}$, and formation of the complex biexciton and dropleton states is possible. According to Fig. 4(a), the role of the *e-h* plasma state increases at higher photoexcitation levels. This makes the localized *e-h* plasmas a significant contributor to the formation of a multishelled quantum droplet structure shown in Fig. 5(c). The degree of *e-h* correlation increases toward the dropleton center and decreases to the electron-hole plasma level at the outer rim of the structure.

Interestingly, the number of rings and the dropleton size both increase with the plasma density, which may be interpreted as size- and particle-number-dependent effects in complex interacting many-body quantum systems that involve *e-h* nanoplasmas. These nanoplasmas are confined in the nanometer-sized GaAs quantum wells and interact with dropletons which effectively set another confinement dimension comparable to their typical radius in the sub-100-nm range. Importantly, the equilibration and the formation of more stable (stronger bonded) quantum states owe to many-body interactions (which involve nanoplasmas) rather than thermalization (Almand-Hunter *et al.*, 2014).

Studies of these exotic states of matter have become possible only recently with the advent of high-precision, high-resolution quantum spectroscopy. Changes in the elemental composition, sizes, and configurations of the quantum wells may lead to interesting size-dependent effects in nanoplasma generation and their interactions with other quasiparticle states. One possible size effect may manifest through the variation of the energy level structure, as in the common case of Si nanocrystals which change their band gap from indirect to direct as their size decreases. The modified energy landscape may affect the effective masses of the carriers, and, hence, their collective plasmalike responses to photoexcitation.

We now consider other situations when nanoplasma states may be generated in photoexcited condensed matter by intensifying the ultrafast radiation which in turn escalates nonequilibrium conditions.

VI. ESCALATING NONEQUILIBRIUM: FROM SOLID TO NANOPLASMAS

As discussed in Sec. III, loosening of ion-ion bonds is an important process in the transition from plasmonic excitations of degenerate electron gas at low radiation intensities (Sec. IV) to nanoplasma states at high radiation intensities (Secs. VI.B and VII). In other words, nonequilibrium should be escalated further compared to the cases considered previously to lead to the transition from solids to plasmas, especially when the solid is not expected to be destroyed as a whole.

Escalating the radiation intensities will lead to much higher energy transferred to the electrons and many more electrons promoted from the valence to the conducting band (this may happen in both dielectrics and semiconductors depending on the energy band gap ϵ_g and the energy of incident photons). Consequently, the electron energy and (upon *e-e* thermalization) temperature may increase significantly. As noted in Sec. II, both λ_{De} and N_D scale similarly with the electron density ($\propto n_e^{-1/2}$) but differently with the electron temperature ($\propto T_e^{1/2}$ and $\propto T_e^{3/2}$, respectively). Hence, by increasing T_e one could achieve higher numbers of electric charges in the Debye sphere even with nanometer-range dimensions.

However, when the radiation intensity increases to $\sim 10^{13} - 10^{15}$ W/cm^2, a significant ($\sim$10%) fraction of electrons is promoted to the CB (Stampfli and Bennemann, 1990, 1992). This may lead to the energy band gap becoming smaller and smaller followed by the transition to the metallic state (Dumitrica and Allen, 2002). As a result, the holes that neutralize electrons in electron-hole plasmas disappear along with ϵ_g. When this happens, the responses of the solids are dominated by the mechanisms that are more relevant to free-electron metals.

In this section we consider *transition processes* that eventually lead to plasma generation in solids confined to nanoscales in at least one dimension. Some of the most important processes include nonthermal lattice disassembly (Sec. VI.A) and the formation of WDM (Sec. VI.B). We also discuss the opportunities to measure collective responses from high-density plasma states (Sec. VI.C) as well as plasma-related effects at the early stages of fs-laser ablation of solid targets (Sec. VI.D) as a possible transition stage of nanoplasma generation from clusters and nanoparticles considered in Sec. VII.

A. Nonequilibrium excitations and athermal phase transitions

When ∼10% of photoexcited electrons are promoted to the CB, atomic bonds in semiconductors loosen through a higher contribution of antibonding states [Fig. 6(a)] (Stampfli and Bennemann, 1992). The fs-laser-induced modification of the electronic density of states is also associated with the phonon frequency changes (Grigoryan, Zijlstra, and Garcia, 2014). These effects become pronounced when the electron temperature reaches $\sim(1-4)\times10^4$ K (a few eV) (Silvestrelli and Parrinello, 1998). The fast nonequilibrium excitation thus leads to hot electron generation in the ion lattice whose energy remains at least 1 order of magnitude lower.

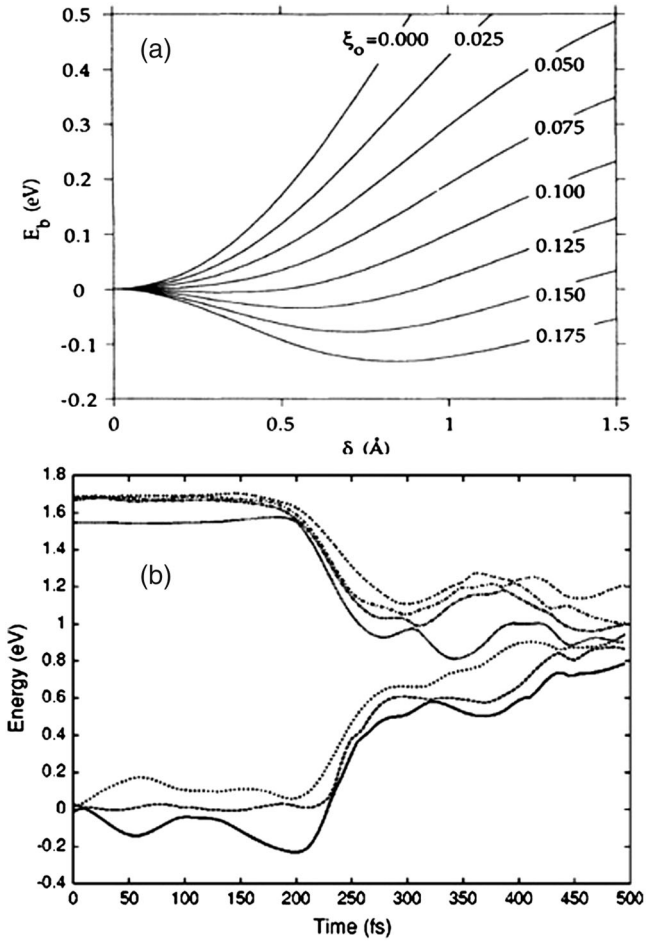

FIG. 6. Responses of semiconductors to fs lasers: (a) bond softening in Si evidenced by the reduction of cohesive energy per bond E_b with the density of the electron-hole plasma ξ_0 at the same amplitudes of the transverse acoustic phonons, and (b) transition of GaAs to the metallic state evidenced by the temporal dynamics of the electronic energy eigenvalues around the band gap at the Γ point. Adapted from (a) Stampfli and Bennemann, 1992, and (b) Dumitrica and Allen, 2002.

Excitation of dense electron-hole plasma induces instability of the diamond structure of C, Si, and Ge (Stampfli and Bennemann, 1990). This electron-hole plasma extends several tens of nanometers deep into the bulk of the samples. This happens within ∼100 fs of the plasma excitation which is much shorter than the time needed for the normal thermal melting. Because of the spatial localization, one deals with transient electron-hole nanoplasmas generated in the near-surface layer of bulk solid materials. When ∼9% of the electrons are excited from the VB to the CB in Si, transverse acoustic phonons become soft, whereas when ∼16% electrons are promoted to the CB, the diamond structure of Si may become unstable (Stampfli and Bennemann, 1990).

The excitation of a large electron fraction across the band gap leads to modification of interatomic forces and ultrafast melting (Rousse *et al.*, 2001). Atoms immediately begin to move and gain sufficient kinetic energy to induce melting. This happens much faster than several ps required to convert the electronic energy into thermal motions. Athermal melting was reported to occur in ultrathin (∼170 nm) Ge layers within 300–500 fs (Sokolowski-Tinten *et al.*, 2001). For comparison, a layer of a few tens of nm thickness typically melts thermally within a few hundred ps. Furthermore, fs-laser radiation induces graphitization of diamond and nonthermal fragmentation of C_{60} (Jeschke, Garcia, and Bennemann, 1999; Jeschke, Garcia, and Alonso, 2002).

Ultrafast time-resolved x-ray diffraction (Rousse *et al.*, 2001) measurements have enabled time-resolved studies of the loss of order in the crystalline lattice with fs resolution. The solid-plasma transitions in InSb occur at the laser fluences $W_{\mathrm{del}} \sim 200$ mJ/cm^2 with the pulse duration of ∼120 fs. Below this threshold, ultrafast nonthermal melting takes place.

Nonthermal melting involves passage through nonequilibrium extreme states of matter (Siders *et al.*, 1999). Optical measurements confirm that intense fs lasers produce dense electron-hole plasmas in semiconductors. These plasmas are characterized through time-dependent reflectivity measurements and are suggested to possibly play a role in nonthermal melting of semiconductors. However, specific mechanisms of the plasma contributions are presently not clear.

As mentioned previously, some semiconductors such as GaAs experience a dramatic reduction of the band gap ϵ_g and transition to the metallic state which happens over sub-ps scales as shown in Fig. 6(b) (Dumitrica and Allen, 2002). Upon this transition, further dynamics of lattice disassembly is governed by the very different mechanisms. Indeed, it is generally accepted that the laser directly excites the electrons in metals which thermalize and reach their electron temperature T_e in a few tens of femtoseconds. Because of the electron-phonon coupling, the energy is subsequently transferred from the electrons to the ions within a few tens of picoseconds leading to the thermal melting of the lattice (Mazevet *et al.*, 2005). This leads to the *different behavior of materials* upon increasing the radiation intensity. For instance, for electronic temperatures up to 6 eV weakening of the

silicon bond induces a lattice instability (similar to some other examples mentioned previously) and gold shows a significant increase of its melting temperature, while any observable effects in Al are much weaker (Recoules *et al.*, 2006).

Atomic motions during ultrafast melting are fundamentally different from those in a fluid. In particular, fractionally diffusive atomic motions can be induced in silicon (Zijlstra *et al.*, 2013). These motions are characterized with unusual temporal dependences of atomic displacements from equilibrium positions $\langle u^2 \rangle = C(t - t_0)^\alpha$, where $\alpha < 1$ and t_0 accounts for nonzero atomic displacements at $t = 0$ and for nondiffusive dynamics at early times. These features further confirm the possibility of highly unusual dynamics of condensed matter under strongly nonequilibrium conditions.

Size-dependent effects may play a role when nonequilibrium is escalated to induce disassembly of a solid lattice. Indeed, melting temperatures of smaller nanocrystals are lower than in their bulk counterparts. These effects may complicate the interplay of equilibrium thermal and nonequilibrium nonthermal mechanisms and require better understanding in the near future. Under certain conditions strongly nonequilibrium phenomena under fast excitation lead to the exotic nonequilibrium states such as the WDM which is regarded as a transition state between the solid and the plasma.

B. Warm dense matter: An intermediate state between solid and plasma

The term "warm dense matter" was introduced in 1999 to call attention to the region of the phase diagram surrounding the solid-plasma transition (Lee *et al.*, 2003; Koenig *et al.*, 2005; Ng *et al.*, 2005; Ng, 2012) by initiating the first International Workshop on Warm Dense Matter (Vancouver, Canada, 29–31 May 2000; Chair: A. Ng). This term refers to states in which the electron temperature is comparable to the Fermi energy and the density of ions is sufficiently high to render Γ_{ii}, the ion-ion coupling parameter (Ichimaru, 1982), greater than unity. Such states are dominated by the complex interplay of electronic excitation, degeneracy, and strong ion-ion correlation. They cannot be described satisfactorily by traditional theories.

Yet the WDM states are prevalent everywhere ranging from materials subjected to intense heating by electric current, lasers, x ray, energetic charged particles, and shock waves to the center of Jovian planets and brown dwarfs. Warm dense matter has since become a new frontier in condensed matter physics and plasma physics, pertinent to studies of matter under extreme conditions, high-energy-density (HED) matter as well as planetary physics (Rosner *et al.*, 2009; Fortov, 2011).

A fundamental challenge in experimental studies of warm dense matter is its high pressure of typically 0.1–10 Mbar. Hydrodynamic expansion readily gives rise to gradients of temperature and density. For the interpretation of experimental data without necessitating the use of hydrodynamic simulations to treat gradient effects, measurements need to be made from a uniform state.

To meet this challenge, the approach of using a uniform slab of nanoplasma produced with *isochoric heating* of an ultrathin foil by an intense fs laser has emerged (Forsman *et al.*, 1998).

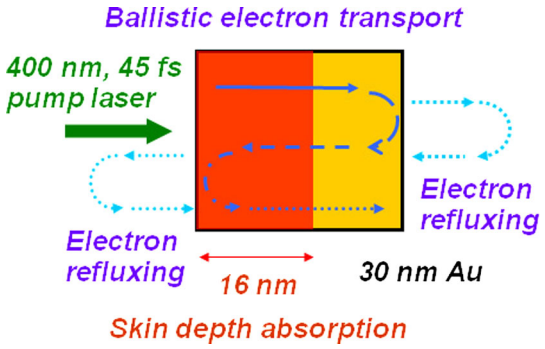

FIG. 7. A schematic diagram of a uniform slab of nanoplasmas produced by isochoric laser heating of a Au nanofoil.

Consider the example of a freestanding, 30-nm-thick Au foil irradiated by a 400 nm, 45 fs laser pulse (Fig. 7). Laser absorption occurs in a skin-depth layer of ~16 nm via photoexcitation of $5d$ electrons to the $6s$ levels. Electron thermalization time is expected to be ~600 fs (Fann *et al.*, 1992) and the ballistic electron range in Au is ~110 nm (Hohlfeld *et al.*, 1997).

Hence, initial energy transport in the foil is dominated by the excited $5d$ electrons moving at Fermi speed of $\sim 10^8$ cm/s. As the work function of Au is ~5 eV, most of the ballistic electrons are reflected at the foil-vacuum interface while the few electrons that escape will be pulled back by the space charge field. With a transit time in the foil of ~30 fs, refluxing of the electrons produces a uniformly heated warm dense matter state long before the excited electrons are thermalized. This approach has become a vital platform for a wide range of studies of nonequilibrium WDM in ultrafast pump-probe experiments. Here we discuss the advances that have been made.

First among these is the discovery of a solid phase at high-energy density. Initial observation from fs-laser heated Au nanofoils reveals a quasisteady behavior in ac conductivity that signals the absence of hydrodynamic expansion (Widmann *et al.*, 2004). Theoretical calculations of ac conductivity yield good agreement with measurement only if the state assumes a solid structure (Mazevet *et al.*, 2005).

The first experimental evidence of the solid phase is obtained from the measurement of broadband (~400–800 nm) dielectric function (Ping *et al.*, 2006). The corresponding lifetime is found from frequency domain interferometry to vary from ~2 ps for an excitation energy density of ~20 MJ/kg (4×10^{11} J/m^3) to ~20 ps for ~0.4 MJ/kg (8×10^9 J/m^3) (Ao *et al.*, 2006). This is consistent with the results of a two-temperature heating-disassembly model that uses an electron-ion coupling factor g_{ei} of $(2.2 \pm 0.3) \times 10^{16}$ W/m^3 K (Hohlfeld *et al.*, 2000) and a fixed-value critical lattice energy density ε_D for lattice disassembly as a free parameter. As shown in Fig. 8(a), the best fit of model to data yields $\varepsilon_D = 0.33 \pm 0.03$ MJ/kg. This is 1.65 times higher than the energy density (including latent heat of fusion) required for the melting of Au under normal conditions, indicative of a superheated solid phase that extends to high-energy densities.

To explain this finding, the mechanism of phonon hardening is deduced from density functional theory–molecular

dynamics (DFT–MD) simulations (Recoules *et al.*, 2006; Kabeer, Zijlstra, and Garcia, 2014). The elevated electron temperature modifies the phonon spectrum causing an increase in Debye temperature that in turn raises the melting temperature. The existence of the solid phase in fs-laser heated Au nanofoils is also corroborated by ultrafast electron diffraction measurements at energy densities of 1.22–2.85 MJ/kg (Ernstorfer *et al.*, 2009). The observed temporal change in intensity of the ⟨220⟩ diffraction peak reveals lifetimes of the solid phase in agreement with that obtained from frequency domain interferometry [Fig. 8(a)]. However, the data have been interpreted using $g_{ei} = (2.2–2.4) \times 10^{17}$ W/m^3 K to corroborate the phonon hardening theory (Recoules *et al.*, 2006), as shown in Fig. 8(b). On the contrary, a recent ultrafast electron diffraction measurement of the ⟨220⟩ diffraction peak reveals much shorter lifetimes of the heated solid phase at substantially lower energy densities, namely, ∼5 and ∼11 ps at 0.37 and 0.23 MJ/kg, respectively (Daraszewicz *et al.*, 2013). Significant loss of absorbed laser energy to the grid structure supporting the Au nanofoil is nonetheless noted.

Next is the benchmark of ac conductivity, a transport property that is of practical as well as fundamental interest. The measurement of ac conductivity of nonequilibrium warm dense Au has initially been derived from the quasi-steady-state reflectivity and transmissivity of the solid phase discussed previously (Widmann *et al.*, 2004). A more precise determination is later obtained from the observation of the state at the time when electron thermalization is first reached (Chen *et al.*, 2013).

The new result provides the first benchmark for testing the *ab initio* model of ac conductivity (Holst *et al.*, 2014). In these calculations, the electron density of states (DOS) is obtained from DFT-MD simulations using the ABINIT code (Gonze *et al.*, 2002). The real part of ac conductivity σ_r is given by the Kubo-Greenwood equation while the imaginary part σ_i is obtained from the Kramers-Kronig relation. As shown in Fig. 9, theory shows good agreement with the experiment when both σ_r and electron heat capacity are evaluated using the electron DOS obtained in ABINIT.

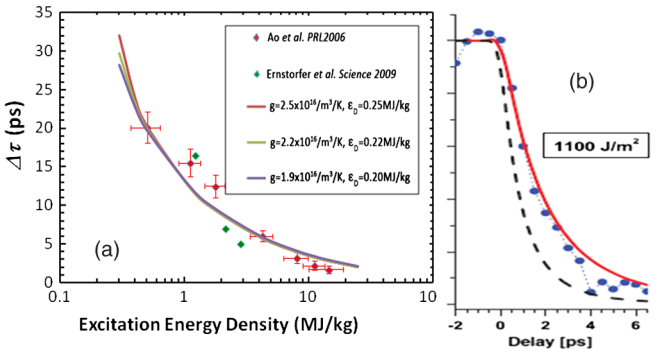

FIG. 8. (a) Lattice disassembly time in a fs-laser heated Au nanofoil. From Ao *et al.*, 2006, and Ernstorfer *et al.*, 2009. (b) Temporal changes in the Debye-Waller factor (Debye, 1913; Waller, 1923) of the ⟨220⟩ electron diffraction peak in fs-laser heated Au obtained experimentally (data points) and by numerical modeling (solid and dashed lines). Adapted from Ernstorfer *et al.*, 2009.

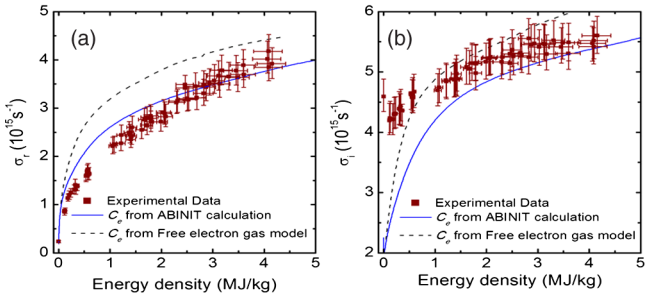

FIG. 9. ac conductivity of nonequilibrium warm dense gold. Adapted from Chen *et al.*, 2013.

On the other hand, σ_i deviates significantly from the measurement at energy density below ∼1 MJ/kg. The discrepancy is traced to missing contributions to σ_r at photon energies below the energy difference (∼0.1 eV) of Kohn-Sham eigenstates in the application of the Kubo-Greenwood equation. This affects the principal value integration within the Kramers-Kronig relation.

In addition, the electron-ion coupling factor g_{ei} has been determined that is central to the understanding of energy relaxation between the two subsystems in nonequilibrium warm dense matter. While the first measurement is made on states in a shock front in Si with hot ions and cold electrons (Celliers *et al.*, 1992; Lower *et al.*, 1998), fs-laser heated nanoplasmas offer new access to states with hot electrons and cold ions.

As noted previously, the measured lifetimes of the solid phase in fs-laser heated Au can be interpreted with $g_{ei} = (2.2 \pm 0.3) \times 10^{16}$ W/m^3 K (Ao *et al.*, 2006), whereas the observed temporal decrease in intensity of the ⟨220⟩ electron diffraction peak (which shows the preferential crystallographic orientation of the Au crystals) can be interpreted with $g_{ei} = (2.2–2.4) \times 10^{17}$ W/m^3 K (Ernstorfer *et al.*, 2009).

Direct determination of g_{ei} was first obtained from changes in the electron temperature derived from x-ray absorption near edge structure measurements on a fs-laser heated target of a 70-nm-thick Cu foil sandwiched between 6-nm-thick carbon layers (Cho *et al.*, 2011). The energy density deposited in the composite target is 3.6 MJ/kg. The frequency domain interferometry measurement reveals the onset of hydrodynamic expansion 5 ps after laser heating. Theoretical absorption spectra near the Cu L_{II} and L_{III} edges are calculated using DFT methods assuming a liquid structure of Cu. The observed temporal decrease in electron temperature over a duration of 20 ps is shown to be in agreement with the calculation using $g_{ei} = 5.3 \times 10^{17}$ W/m^3 K derived from DFT (Lin, Zhigilei, and Celli, 2008); see Fig. 10(a).

More recently, g_{ei} in fs-laser heated Au nanofoils has also been determined from the temporal change in ac conductivity when the states remain in the solid phase (Chen *et al.*, 2013). The measured values of σ_r are compared with that calculated from the Kubo-Greenwood formulation using electron DOS derived from DFT-MD simulations (ABINIT) and a two-temperature model incorporating different g_{ei}. The rate of change in σ_r calculated with g_{ei} derived from DFT deviates significantly from the measurement but there is good agreement for calculations assuming g_{ei} of 2.2×10^{16} W/m^3 K, as

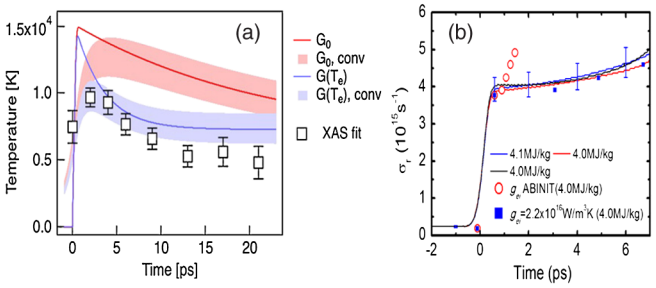

FIG. 10. (a) Temporal evolution of electron temperature of fs-laser heated Cu. Adapted from Cho *et al.*, 2011. For the electron-ion coupling factors, $G_0 = 10^{17}$ W/m^3 K and $G(T_e)$ is calculated using DFT (Cho *et al.*, 2011). The shaded curves include the experimental accuracies in absorbed energy density and the temporal resolution of the detector. (b) Temporal evolution in ac conductivity of fs-laser heated Au. Adapted from Chen *et al.*, 2013.

presented in Fig. 10(b). These studies are driving the re-examination of the ion density spectral function used for the calculation of g_{ei} in DFT-MD methods.

Notably, a unique aspect of warm dense matter is its duality as a condensed matter and a plasma state. The former is well illustrated by the nonequilibrium solid phase and the phenomenon of phonon hardening. The latter can be found in the measurement of x-ray scattering from plasmons in nanosecond-laser heated bulk targets of beryllium (Glenzer *et al.*, 2007) (see Sec. VI.C for more details). This dual nature adds both intrigue and challenge to warm dense matter research.

C. Collective responses in high-density plasma states

As discussed in Sec. IV, excitation of collective plasmalike (plasmon) responses under resonant (plasma resonance) conditions in nanometer-sized solids is a reliable way to study size-dependent effects of nanoscale confinement of both electrons and photons. On the other hand, detection of plasma resonances can be used as evidence for collective oscillations in high-density plasmas. Similar to the establishment of screened Coulomb potential and collective plasma responses in photoexcited semiconductors through plasmon detection (Sec. V.A), the study of plasmonic responses under intense radiation conditions can be used to confirm collective motions that are attributed to the plasma states.

Because of the transient nature of the plasma states under intense radiation conditions, such measurements are quite challenging for nanoplasma states generated in nanometer-sized solids. However, successful recent studies of plasma parameters in warm dense matter generated in bulk samples (e.g., using shock compression) open an opportunity to conduct similar measurements for nanoplasma states produced by irradiation of nanometer-thin metal foils by intense fs-laser radiation discussed in Sec. VI.B.

Indeed, the study of plasmon responses from WDM allows one to estimate the electron number density from the measured frequency shifts associated with plasmon excitations. The plasma parameters have been measured and calculated for warm dense beryllium (Glenzer *et al.*, 2007). The typical values for n_e and T_e are $(1–2) \times 10^{23}$ cm^{-3} and 10–15 eV, respectively. The electron energies are therefore of the order of the Fermi energy.

The energy associated with the plasmon excitation is $\Delta E_{\rm pl} = \hbar\omega_{\rm pl} \sim 28$ eV, which is a few orders of magnitude higher compared to low-irradiation-intensity plasmonics in Sec. IV and electron-hole plasmas in Sec. V. Here

$$\omega_{\rm pl}^2 = \omega_p^2 + 3(kV_{Te})^2(1 + \xi n_e \Lambda_e^3) + \left(\frac{\hbar k^2}{2m_e}\right)^2, \qquad (16)$$

where ω_p ($\hbar\omega_p \sim 20$ eV) is the plasma frequency (4), $V_{Te} = (k_B T_e/m_e)^{1/2}$ is the electron thermal velocity, k is the wave number, $\Lambda_e = \sqrt{2\pi}\hbar/(m_e k_B T_e)^{1/2}$ is the thermal wavelength, and $\xi = 0.088$ (Glenzer *et al.*, 2007). Equation (16) includes terms related to plasma oscillations, spatial dispersion, degeneracy-related correction, and quantum diffraction of the electrons. However, finite-size geometry effects of the samples are not included.

Another signature of collective plasma responses is related to the level of collision losses (some mechanisms relevant to low-radiation-intensity plasmonics have been discussed in Sec. IV). Such responses have been measured and explained using shock compression of solid matter (boron) by high-energy (250 J energy, $I_{\rm rad} \sim 10^{17}$ W/cm^2) laser pulses of 10 ps duration (Neumayer *et al.*, 2010). This compression produces strongly coupled, very dense ($n_e \sim 4 \times 10^{23}$ cm^{-3}) plasmas, which show moderate (~0.2 eV) electron temperatures and a high level of collisional losses. The energy $\Delta E_{\rm pl} \sim 32$ eV associated with the excitation of collision-dominated plasmons is ~4 eV higher than in the previous case of warm dense beryllium. Under such conditions, the plasma is Fermi degenerate ($k_B T_e/E_F \sim 0.01$, where E_F is the Fermi energy), while the very high densities and relatively low electron temperatures render the concept of Debye length not applicable. Even though well-resolved collective plasma responses are generated, the properties of the plasmons detected by k-vector and frequency resolved x-ray Thompson scattering are determined by electron-ion collisions, below certain critical wave numbers k_c when the plasmons merge with the single-pair continuum giving rise to Landau damping (Neumayer *et al.*, 2010).

The presence of quantization [Eq. (16)] and energy dissipation-related terms in plasmon dispersion measured from the WDM states with the electron density and temperature that are quite similar to the cases considered in Secs. VI.B and IX suggests that account of finite-size effects (e.g., by imposing boundary conditions that will affect scattering, losses, etc., in nanometer-thin metal foils or nanostructure arrays) where nanoplasmas are produced, may lead to interesting size-dependent effects, possibly similar to the low-radiation-intensity plasmonics (Sec. IV). One could thus anticipate more studies related to size-dependent collective effects in nanoplasma generation in the near future.

D. Plasma effects in fs-laser ablation

As mentioned in Sec. VI.A, transient electron-hole nanoplasmas localized to very thin (typically tens to 100 nm) layers near the surface are formed upon irradiation of semiconductors and dielectrics with intense fs lasers. These plasmas are formed

by ionization at early exposure stages and play a role in femtosecond laser ablation of solid targets as discussed later.

Ionization is one of the most intrinsic and universal effects that lead to plasma production. Intense fs-laser pulses of $I_{rad} \sim 10^{13}$–10^{14} W/cm^2 are able to ionize dielectric targets very rapidly. The fields of these and higher intensities are able to deliver the energy exceeding the binding energy of atoms and release them from the target (Gamaly *et al.*, 2002). The electrons produced at the beginning of the excitation pulse interact with photons and absorb laser energy.

Electron impact and multiphoton ionization are among the most important mechanisms of ionization in intense laser fields. The relative importance of these ionization mechanisms depends nonlinearly on I_{rad}. When I_{rad} is sufficiently high (e.g., $\sim 10^{14}$ W/cm^2 for SiO_2), the importance of multiphoton ionization becomes higher, and the target can be ionized within a few tens of fs. When the ionization is complete, the plasmas are formed in the skin layer of the target (typically a few tens of nm). These nanoplasmas feature electron densities $\sim 10^{23}$ cm^{-3}, comparable to the ion density in the solid, thus exhibiting high ionization degrees.

Importantly, very effective ionization of dielectrics creates a nonideal and very dense electron gas with the energy of Coulomb interactions being comparable with the thermal energy; in this case $N_D \leq 1$. This electron gas dominates photon absorption, very similar to free electrons in metals. The key mechanisms leading the electron energy increase are related to the inverse bremsstrahlung and resonant absorption mechanisms (Gamaly *et al.*, 2002). The latter happens when the electron density increases so that the excitation frequency ω becomes resonant with ω_p. As discussed in Sec. VII, this resonance condition plays a prominent role in the interaction of intense laser radiation with nanoscale solid objects leading to nanoplasma generation.

If the electron energy exceeds the work function of the material, they can escape from the target. This causes separation of the electrons from ions well before they exchange energy (which requires at least a few hundred fs as discussed in Sec. VI.A). If the electron energy is higher than the binding energy of ions in the lattice, the resulting electric field pulls the relatively cold ions out of the target and the plasma expands beyond the target surface.

The specific effect of radiation on solid materials is determined by the amount of radiation energy absorbed, for example, per atom or unit mass of the material. For example, the dynamics of structural instabilities and disassembly of graphite induced by fs-laser excitations is very different just above the damage threshold (>2.0 eV/atom) and high absorbed energies of >3.3 eV/atom (Jeschke, Garcia, and Bennemann, 2001). In the former case graphite ablation occurs via removal of intact graphite sheets, while in the latter case nonequilibrium melting is followed by fast evaporation. Further details of the specific mechanisms and thresholds of ablation of solids with fs lasers can be found in the original work of Gamaly *et al.* (2002) and references therein. Ablation of bulk targets using fs lasers has been widely discussed in the literature (Willmott and Huber, 2000; Juodkazis *et al.*, 2006; Kabashin *et al.*, 2010) and is outside the scope of this Colloquium.

These effects are relevant and bring new interesting physics when the size of the solid targets is reduced to the nanometer range. This case when nanoplasmas are produced by intense irradiation of nanoscale targets such as atomic clusters and small nanoparticles is considered next.

VII. NANOPLASMAS FROM IRRADIATED CLUSTERS AND NANOPARTICLES

When clusters or small nanoparticles are irradiated with fs lasers with $\sim 10^{14}$–10^{17} W/cm^2 intensity, electrons escape and nanoplasma is created around these objects, as discussed in Sec. VI.D. This happens over the time scales comparable with the fs pulse duration (Kohn, Redmer, and Fennel, 2012).

In this case, strong electric fields are generated in the vicinity of the clusters and nanoparticles and are determined by the local laser field intensity and the (nanometer) geometric features (e.g., radius of curvature) of the irradiated nanoscale objects. These effects increase the contribution of the tunnel ionization (Ditmire *et al.*, 1996) compared to the collisional and multiphoton ionization involved in the ablation of bulk targets (Sec. VI.D). The important feature of this case is

$$\lambda^{fs} \gg \lambda_{skin} \sim d_{cl}, \tag{17}$$

where λ^{fs} is the fs-laser wavelength, λ_{skin} is the skin depth of the optical field, and d_{cl} is the cluster or particle size. This opens opportunities for the studies of size-dependent effects, which could involve nanoplasmas.

When more and more electrons are produced within and around the near immobile ion background of the clusters, the plasma density increases until the laser frequency becomes resonant with the local plasma frequency $\omega = \omega_p$. This leads to the dramatic increase of the energy absorbed from the laser. The plasmas that are composed of a relatively small number (e.g., $\sim 10^4$) of electrons and ions (D'Angola, Boella, and Coppa, 2014) are confined around the nanoclusters, which expand due to the continuously increasing hydrodynamic pressure and Coulomb repulsion between the ions in the cluster. Eventually, these processes lead to Coulomb micro-explosions, shock wave formation, and rapidly expanding plasmas.

Interestingly, the number of electrons and the rates of their release from the clusters or small nanoparticles depend on their material and size. Consequently, the specific moment of time and location of the plasma resonance $\omega = \omega_p$ may be different depending on the composition, size, and shape of the irradiated objects. The plasma density is affected by the electrons released from the inner shells of atoms, which become multicharged. For example, very high-Z charged states such as Ar^{16+} have been reported (Rozet *et al.*, 2001). Vacancies (holes) are thus created in the inner shells of the atoms and hot electrons with kinetic energy in the keV range are ejected. The higher electron energies lead to larger N_D, and the plasma may satisfy the weak coupling and ideality conditions, even for λ_{De} in the nanometer range.

Ionization processes leading to nanoplasma production are very efficient and may lead to complete stripping of atoms of all their electrons. This was demonstrated by adding a small number of xenon atoms to helium droplets (Mikaberidze,

Saalmann, and Rost, 2009). The addition of xenon atoms enables new effects which are different for the resonant and nonresonant excitation wavelengths as shown in Fig. 11(a). Figure 11(b) shows that the addition of a seed cluster of just 13 Xe atoms can lead to the extremely effective avalanche ionization of He clusters containing up to 10^5 atoms, virtually all to the He^{2+} charged state. Importantly, this effect is observed only for $\lambda = 780$ nm. Moreover, the pristine He droplet cannot be ionized even at significantly higher I_{rad}. This phenomenon was explained by initial field ionization of the Xe_m seed clusters, which produced a very high electric field and led to the enhanced ionization of He atoms. As the electron density increases, localized resonant absorption in nanoplasmas with elongated geometry [Fig. 11(c)] takes place. The first-approximation estimate for the resonant condition (and the corresponding nanoplasma density) can be obtained using Eq. (5) (Mikaberidze, Saalmann, and Rost, 2009). This resonance is excited nearly instantly, within a few fs into the laser pulse. Laser excitation at $\lambda = 200$ nm is nonresonant and produces ionization predominantly through the laser field-related mechanism.

This mechanism revealed by microscopic calculations has been validated experimentally (Krishnan *et al.*, 2011). Consistently with the results shown in Fig. 11(a), these experimental results reveal that less than 10 dopant atoms are sufficient to generate nonspherical nanoplasmas sketched in Fig. 11(c) by using intense 10 fs-laser pulses.

Nanocluster-size-dependent effects are important for the inner-shell high-order ionization processes that lead to x-ray generation (typically in a few keV range) (Micheau, Jouin, and Pons, 2008). As shown in Fig. 11(d), clusters of the radius of ~40 nm produce the strongest x-ray emissions when the laser pulse duration is fixed.

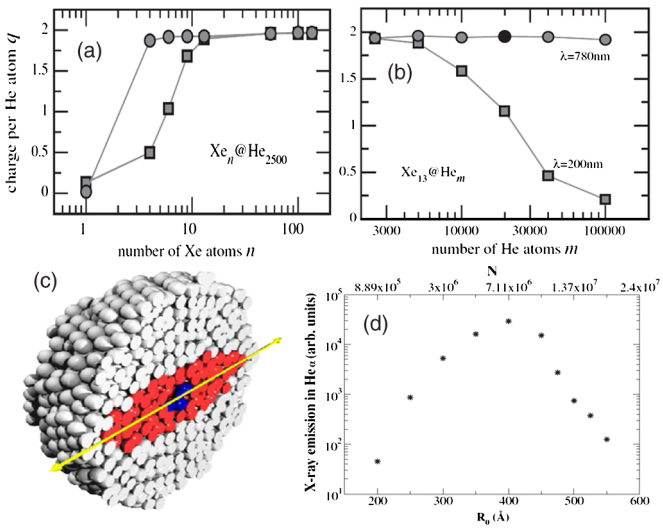

FIG. 11. Effects of cluster size and anisotropy in nanoplasma generation. (a), (b) Charge per He atom for He droplets of 2500 atoms with Xe_n cores vs the number (a) n of Xe dopant atoms and number of He atoms (b) m in the droplet for Xe_{13} core, at a laser intensity of 7×10^{14} W/cm^2. (c) Anisotropic cross section of the Xe core and the nanoplasma around it, within the He droplet; the arrow shows the laser polarization. (a)–(c) Adapted from Mikaberidze, Saalmann, and Rost, 2009. (d) Intensity of He_α emission line vs initial Ar cluster size for 300 fs-laser excitation with 1.6×10^{16} W/cm^2; N is the number of atoms in the cluster. Adapted from Micheau, Jouin, and Pons, 2008.

As mentioned, later stages of nanoplasma dynamics feature shock waves, which have only recently been confirmed experimentally. Imaging the momentum distribution of individual, isolated 100-nm-scale plasmas was used to observe the shock waves in nanoplasmas produced by 40 fs-laser pulses with $I_{rad} = 3 \times 10^{13}$–$4 \times 10^{14}$ W/cm^2 (Hickstein *et al.*, 2014). An interesting size-dependent effect was observed—larger nanoparticles were more likely to form shock waves. Indeed, larger nanoparticles are likely to produce denser and larger nanoplasmas which in turn would absorb more energy from the laser field. The expansion of the nanoplasmas into vacuum (over ~6 ps) is slower compared to the cases involving smaller clusters and nanoparticles. However, the density-dependent energy absorption due to plasma resonance upon expansion is quite similar to the He droplet case discussed previously.

Nanoplasmas can also be generated by irradiation of small clusters with intense extreme UV (EUV) radiation (Wabnitz *et al.*, 2002; Bostedt *et al.*, 2008). This radiation can be produced using free-electron lasers in the soft-x-ray regime with the wavelengths well under 100 nm. Shorter and shorter wavelengths are becoming available with the advent of new devices. In this energy range (> 10 eV), photon energy often exceeds the ionization potential of atoms, and the physics of interaction of the short EUV pulses with nanoclusters becomes very different compared to the above examples where light sources of much lower [e.g., in the near-infrared (NIR) range] energy are used. In this case, multistep photoionization of clusters (accompanied by direct electron emission) becomes the dominant energy absorption process, whereas the plasma heating has no significant effect, for example, during the interaction of fs EUV ($\lambda = 32.8$ nm) pulses with argon clusters of ~100 atoms (Bostedt *et al.*, 2008). The nanoplasmas are formed through the charge buildup which frustrates the direct electron emission, followed by Coulomb explosion of the cluster. Thus, the dynamics of nanoplasma formation is quite different compared to the NIR excitation case discussed previously.

The nanoplasmas produced by intense irradiation of nanoscale solid objects are typically weakly coupled ($\Gamma_j \ll 1$) and collisions do not significantly affect the phenomena occurring on a time scale of the order of the inverse of the plasma frequency: $\nu_{ee}/\omega_p \sim 10^{-2}$–$10^{-3}$ for T_e in the range 10^2–10^3 eV (D'Angola, Boella, and Coppa, 2014).

Therefore, relatively weakly damped collective plasma effects (e.g., waves) may play a role in the laser-nanocluster interactions. For example, plasma-wave processes developing at attosecond scales in small (with the radius of 30 nm) nanoclusters significantly affect the laser energy absorption mechanisms (Varin *et al.*, 2012). Importantly, due to the spatial localization of the plasma phenomena, interesting size-dependent effects may appear. For example, wave propagation across the clusters may limit the light absorption efficiency when the cluster size exceeds a certain threshold.

Nanoplasmas of this section represent an interesting object for laboratory research and applications because they offer enhanced laser absorption compared to solid or gas targets,

enabling high-energy physics with tabletop-scale lasers. For example, explosion of deuterium nanoclusters using small-scale, high-repetition-rate tabletop lasers may lead to the generation of ions with the energies in the MeV range, the ignition of fusion reactions, followed by the generation of up to 10^5 fusion neutrons per joule of the laser energy input (Ditmire *et al.*, 1999). This breakthrough may lead to the development of ultracompact neutron sources with diverse applications in energy, materials, and other fields. Some other possible applications are considered in Sec. IX.

VIII. OTHER POSSIBILITIES

We now briefly consider some other typical situations where the generation of nanoplasmas may be possible without irradiation of matter with intense femtosecond lasers. Two of these examples correspond to the near and in solids cases followed by a theoretical prediction of nanoplasmoid states.

Nanoplasma generation is possible near solids within thin waveguides with nanometer dimensions cut in Au and filled with Ar (Sivis and Ropers, 2013); see the inset in Fig. 12. Excitation by low-intensity ($\sim 5 \times 10^{11}$ W/cm^2 8-fs pulses, 800 nm wavelength) is used to concentrate strong near fields within the narrow waveguide gaps. This effect is very similar to the localized near-field enhancement near the edges of nanostructures (Sun *et al.*, 2013) in low-radiation-intensity plasmonics shown in Fig. 2(e). The formation of Ar plasmas confined within submicrometer-sized holey Au waveguides is confirmed by the EUV fluorescence measurements (Sivis and Ropers, 2013).

The collective aspects of the plasma dynamics are further evidenced by the hysteresis of the optical excitation with respect to the incident laser intensity (Fig. 12). Interestingly, this behavior is waveguide size and geometry and gas-pressure dependent. These hysteresis phenomena reflect nonlinear, bistable system behavior and have been related to cascaded excitation of nanoplasmas and microplasmas by concentrating optical fields in microstructured holey plasmonic waveguides. A quite similar cascaded excitation was proposed to explain bistable behavior of high-density inductively coupled plasma discharges in Ar and other gases (Ostrikov, Xu, and Lee, 2000).

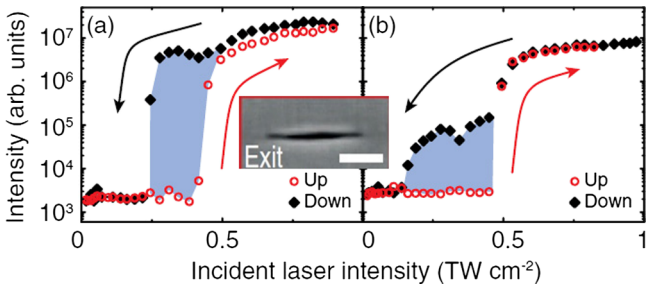

FIG. 12. Bistability of the intensity of excitation of a 104.8 nm line of Ar in two different holey and tapered waveguides with submicrometer dimensions of cross sections drilled in Au (an exit aperture with an elliptical cross section is shown in the inset, scale bar is 200 nm). Adapted from Sivis and Ropers, 2013.

An interesting example of nanoplasmas created in solids is related to the localization of plasmas within ion tracks created upon interactions of fast heavy ions with solids. These plasma channels are created by single energetic (projectile) ions slowing down in condensed matter and typically have lateral dimension of a few nanometers (Faenov *et al.*, 2009). These states are transient and feature ultrafast multistage relaxation within tens of fs, while typical plasma lifetimes τ_{plasma} are of the order of several hundred fs.

For example, the nanoplasmas produced by Mg^{7+} projectiles impinging on the Al target with the energy of 3 MeV/amu feature $n_e \sim 4 \times 10^{23}$ cm^{-3}, $T_e \sim 40$ eV, and $N_D \sim 0.69$. These plasmas are strongly coupled ($\Gamma_j \sim 0.43$) but nondegenerate ($\Theta \sim 0.033$) (Rosmej *et al.*, 2005; Faenov *et al.*, 2009). The nanoplasma relaxation models help one to understand the dynamics of heavy ion track evolution which involves overheating of ion lattice, generation of hot electrons, two-temperature hydrodynamic motions, shock wave generation, etc. These phenomena are qualitatively quite similar to the ultrafast dynamics of fs-laser-induced excitations leading to the formation of WDM and nanoplasmas discussed in Secs. VI and VII.

In the examples presented in this Colloquium, nanoplasmas represent short-living transient states, which leads to the question if it is possible to generate stable nanoplasmas, perhaps in a way similar to natural long-living plasma structures such as ball lightning. Theoretical calculations suggest that stable quantum plasmoids may exist below the critical size of ~10 nm, when the electron-electron interaction becomes attractive and strongly coupled bound electron-electron states may form, similar to Cooper pairs in metals (Dvornikov, 2011). Estimates show that these intricate phenomena may happen at electron densities of the same order of magnitude ($n_e \sim 10^{23}$ cm^{-3}) as in many other cases considered in this Colloquium. However, this theoretical prediction was made at temperatures $\sim 10^3$ K, which are well below the temperatures characteristic to WDM and nanoplasma states considered in Sec. VI. These results motivate further studies of quantum plasmas (Marklund and Shukla, 2006) and their properties at the nanoscale.

IX. POTENTIAL APPLICATIONS

Several interesting properties of nanostructured targets make them attractive for a range of applications, including creation of dense hot plasmas with a temperature of 2–4 keV, efficient x-ray and ion sources. Nanostructured targets are of particular interest because they improve coupling of laser energy to the target (Cristoforetti *et al.*, 2014). This approach may enable novel sources of high-energy particles (e.g., ions in exotic highly charged states), light, and magnetic fields (Rosner *et al.*, 2009).

The highly unusual excited states (e.g., with holes arising from removal of electrons from inner electron shells) of matter may exhibit unprecedented reactivity. Moreover, the associated x-ray emission with specific wavelengths (e.g., corresponding to the generation of Ar^{13+}, Ar^{14+}, Ar^{15+}, etc., ions during nanoplasma formation from irradiated nanoclusters) may be used for the development of ultracompact synchrotrons and x-ray lasers (Rosner *et al.*, 2009).

On the other extreme, control of electron-hole plasmas and associated exotic quasiparticle states in semiconductor quantum wells may lead to the next-generation quantum nanodevices with precisely tunable properties determined by the interplay of photonic (photoexcitation) and electronic effects. Study of the quantum plasmonic properties of these and artificially designed nanometamaterial structures featuring nonlinear effects (Lapine, Shadrivov, and Kivshar, 2014) may further enhance our ability to control light at subwavelength dimensions and to expand the accessible wavelength ranges. Next we briefly discuss two different applications that are related to the production and confinement of plasma states at microscales and nanoscales.

A. Nanoscale synthesis and processing

The first example refers to using fs-laser-induced microexplosions within transparent solids to produce microvoids and novel, structurally unique crystalline and amorphous nanomaterials (Gamaly *et al.*, 2012, 2013; Buividas *et al.*, 2014). When a beam of a fs tabletop laser is focused onto a submicrometer spot within a transparent (e.g, sapphire, Al_2O_3) crystal, the arising highly concentrated power produces confined microexplosions in the solid, leading to transient plasmalike states confined within the voids with the sizes in the few hundred nanometer range as shown in Fig. 13. By steering the position of the initial focus within the crystal, it is possible to form regular patterns of the voids. The electron density of the microplasmas generated is also in the $\sim 10^{23}$ cm^{-3} range. According to Gamaly and co-workers (Gamaly *et al.*, 2012, 2013), this plasma is strongly coupled and nonideal ($N_D \sim 0.84$–1.0), while conditions for the formation of WDM states are satisfied.

The dynamics of microexplosions within solids (Gamaly *et al.*, 2013) shows several features and phenomena (e.g., concentration of laser energy) that are quite similar to Coulomb explosions and shock formation during the interaction of intense laser beams with clusters and small nanoparticles discussed in Sec. VII. However, the localized confinements to submicrometer (and potentially even smaller) dimensions are truly unique features of the microexplosions and the arising high-energy-density states. This interesting aspect deserves further exploration in the near future.

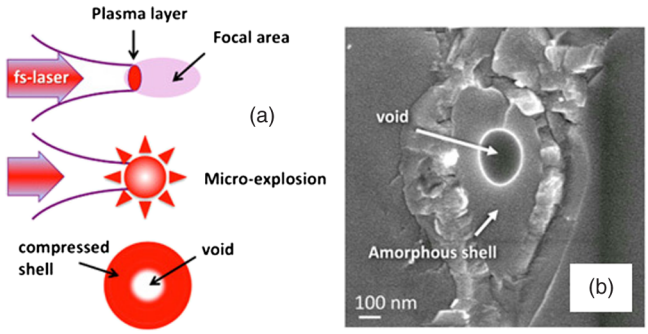

FIG. 13. Dynamics of confined microexplosion in (a) sapphire leading to (b) plasmalike state formation in microvoids induced by a fs-laser pulse. Adapted from Gamaly *et al.*, 2012.

In these experiments a very high-energy density of ~ 2.4 MJ/cm^3 leads to dissociation of Al_2O_3, followed by the removal of 3–4 electrons from Al and O atoms. Under such conditions, the electron temperature can reach ~44 eV, and enormous pressures in the TPa range lead to superdense body-centered-cubic Al, whereas under normal conditions Al adopts the face-centered-cubic structure (Vailinois *et al.*, 2011).

Further examples of structural transformations in materials induced by focused microexplosions include changing of iron valence states and the formation of mixed nanocrystalline and amorphous states in olivine [$(Mg, Fe)_2SiO_4$], which is one of the most abundant minerals on the Earth, the Moon, and Mars (Buividas *et al.*, 2014). Exposure of this mineral to confined microexplosions may lead to the effective separation of Fe from the lighter constituent elements Mg, Si, and O. This finding may provide the mechanism of the formation of the iron-rich core of the Earth during its early evolution stage (Gamaly *et al.*, 2012). Further reductions of energy deposition and plasma confinement areas in size may possibly lead to new interesting effects including exotic properties of the arising nanomaterials.

Intense laser-produced microplasmas offer other interesting opportunities for nanoscale processing of materials. For example, microplasma-based sources of EUV radiation promise applications in high-volume, scalable nanomanufacturing, in particular, by using 13.5 nm EUV radiation for nanolithography (EUV lithography, 2015).

B. Subrelativistic and relativistic nanoplasmas

The physics of subrelativistic and relativistic nanoplasmas is a new emerging field of research. The interaction of short-pulse high-intensity lasers with nanostructured targets has generated strong interest owing to the many potential applications from intense x-ray sources to efficient ion generation and creation of extreme states of matter (pressures in the range of 2 Gbar and energy density of the order of 2 GJ/cm^3). These excitation parameters have been made possible by the use of nanostructured targets which enable much higher laser energy coupling to the targets compared to ~30%–40% (or even lower) offered by conventional targets (Cristoforetti *et al.*, 2014).

Initial work with the use of nanometer-sized wires showed that relativistic electrons in several MeV energy range can produce mega-Gauss (hundreds of Tesla) magnetic fields. In these experiments, 60 nm in diameter and 600 nm long silica-coated Si NWs were irradiated by high-intensity (3×10^{18} W/cm^2), 30 fs, 800 nm laser pulses (Singh *et al.*, 2012). The amorphous shell ensures effective light absorption while the photoexcited crystalline core provides the path for the return current (Bell *et al.*, 1997). Upon irradiation with the fs-laser beam of such a high intensity, the target is instantly ionized, with the electrons escaping the nanowires. Near the sharp nanowire tips, these electrons encounter the much amplified electric field, with the estimated enhancement factor of 11, which corresponds to the 121-fold local increase of I_{rad}.

According to the scaling law $T_e \sim I_{\mathrm{rad}}^{1/3}$ (Forslund, Kindle, and Lee, 1977; Beg *et al.*, 1997), the temperature of the generated hot electrons increases in approximately 5 times.

This can be seen in Fig. 14(a) which shows the two populations of hot electrons, with $T_e = 1754$ keV corresponding to Si NWs and $T_e = 332$ keV to silica target. Furthermore, the fast electron penetration depth into Si NWs is ~16 times higher than in silica, which facilitates the effective return current transport. The mega-ampere current generated in these experiments much exceeded the Alfvén limit (~17 kA for the 1 MeV electron beam) (Alfvén, 1939; Singh *et al.*, 2013). The resulting magnetic fields for Si NWs reach 55 MGs (5.5×10^3 Tl) and are ~18 times higher and decay nearly twice slower compared to the bulk silica target.

Similar effects have been demonstrated for other nanostructured materials such as Cu nanowire-filled nanoporous anodized aluminum oxide templates (Singh *et al.*, 2013). The increase of the hot electron energy and current was attributed to the nanoplasma generation in Cu NWs, in part because of the higher conductivity of the Cu plasma arising from more effective ionization compared to the bulk target. This leads to the fast and unimpeded electron transport through the nanowire needed to maintain the return charge neutralizing current.

The effects of nanometer size on the efficiency of ionization and nanoplasma generation deserve thorough experimental and theoretical studies. These studies may further clarify the key processes inside and on the surfaces of the Si and Cu NWs during the interaction with intense laser pulses. We emphasize that high-intensity ($>10^{18}$ W/cm^2), ultrashort (30 fs) laser pulses generate significant populations of relativistic electrons, such as the electrons with $T_2 = 1.754$ MeV in Fig. 14(a).

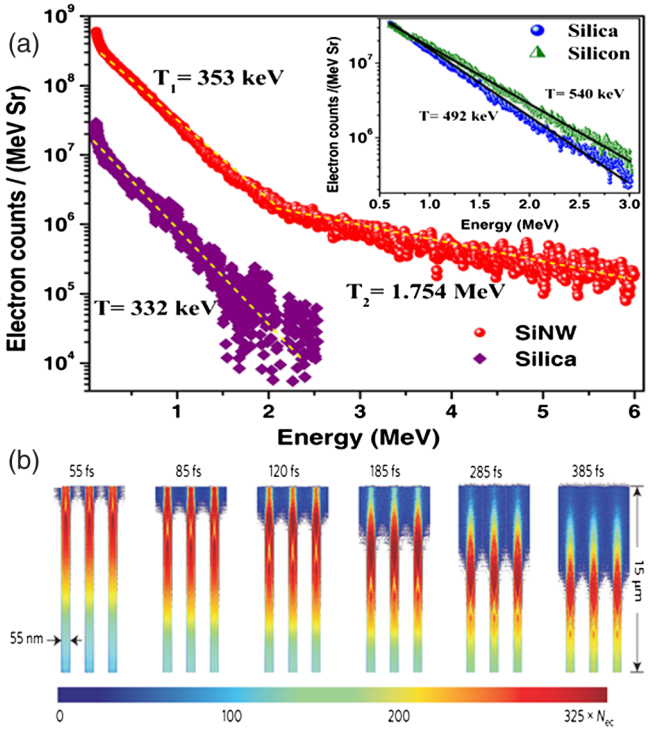

FIG. 14. (a) Energy spectrum of hot electrons emitted by Si NWs and bulk silica target at $I_{\rm rad} = 3 \times 10^{18}$ cm^{-2}. The inset shows similar spectra for bulk silica and silicon at a higher intensity $I_{\rm rad} = 5 \times 10^{18}$ cm^{-2}. Adapted from Singh *et al.*, 2012. (b) Dynamics of electron density (expressed in units of n_{ec}) in nanoplasmas excited in 55-nm-thin, 15-μm-long Ni nanowires. Adapted from Purvis *et al.*, 2013.

Other works with nanostructured targets (nanowires) showed the efficient (bremsstrahlung and $K\alpha$) x-ray sources with yields an order of magnitude higher compared to conventional targets (Kahaly *et al.*, 2008; Bagchi *et al.*, 2011; Chakravarty *et al.*, 2011). Enhancement in x-ray yield is attributed to the higher absorption of laser energy into nanostructured targets. The higher laser absorption could be due to the enhanced local electric fields, plasmonic resonances among other factors (Cristoforetti *et al.*, 2014).

Perhaps the most important effect pertinent to nanowires is that they help to increase the depth of laser energy absorption compared to common targets, where the penetration depth is determined by the critical electron number density n_{ec} determined from the plasma resonance condition $\omega = \omega_p(n_{ec})|_{S_c}$ which is satisfied on the critical surface S_c. In the case of vertically oriented metal nanowire arrays the critical surface can be extended from the usual skin depth in bulk materials (see Sec. VI.D) to several micrometers deep into the target thus leading to the effective volumetric absorption (Purvis *et al.*, 2013).

The effective ionization and volumetric heating of vertically aligned nanowires creates near-solid-density nanoplasmas with keV electron temperatures. In these experiments, Au and Ni nanowire arrays were irradiated with a 0.5 J, 60 fs laser of 5×10^{18} W/cm^2 intensity (Purvis *et al.*, 2013). Upon laser exposure, hot electron-impact ionization leads to the plasma expansion along the depth of 55-nm-thick, 15-μm-long nanowires where the electron density can become more than 100 times higher than $n_{ec} = 7 \times 10^{21}$ cm^{-3} and even reach $n_e = 2 \times 10^{24}$ cm^{-3} as shown in Fig. 14(b) (left panels). The hot plasma propagates inside the nanowires toward the substrate until it expands into the space between the nanowires [see the right panels in Fig. 14(b)]. At this point, the critical surface forms thus effectively stopping laser propagation, and a plasma with near-solid density $n_e = 3 \times 10^{23}$ cm^{-3} and extraordinarily high ionization degree (e.g., containing Au^{52+} ions) is generated.

Importantly, the very low amount (0.5 J) of energy deposited into the nanowires generates thermal energy density of 2 GJ/cm^3 with an average electron thermalized energy of 4 keV over the penetration depth. Calculations show that the wire core reaches an unprecedented thermal pressure of 10 Gbar; after the plasma expansion, the thermal energy density and pressure are ~0.3 GJ/cm^3 and 1–2 Gbar, respectively (Purvis *et al.*, 2013).

Similar extremely high pressures are generated in the central hot spot of laser implosion of fusion capsules in inertial confinement experiments at the National Ignition Facility equipped with the worlds most powerful laser with an estimated energy of 2 MJ (Glenzer *et al.*, 2012). The use of nanowires or nanostructured targets with small (e.g., 0.5 J, 60 fs) lasers can therefore create matter under extreme conditions that are otherwise possible only by using the most powerful lasers. This opens up an exciting opportunity to study the exotic ultradense hot matter by combining small-scale lasers with nanostructured targets (see Fig. 15). For

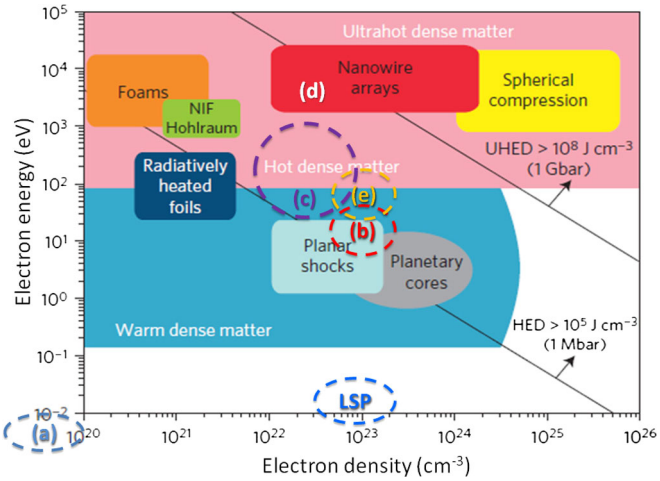

FIG. 15. Ultrahigh electron energies and densities achievable through high-intensity irradiation of oriented nanowire arrays in comparison to other high-energy-density (HED) plasmas. Through this approach, the parameter region of ultrahigh-energy densities (UHED) exceeding $\sim 10^8$ J/cm^3 may be accessible. Approximate parameter spaces corresponding to localized surface plasmons (LSP) of Sec. IV and nanoplasma examples (a)–(e) summarized in Fig. 1 are also marked for comparison. The sizes of the dashed circles and ovals are not to scale and represent only the approximate locations of the nanoplasma cases considered in this Colloquium, with respect to other plasmas that feature moderate, high-, and ultrahigh-energy densities. Adapted from Purvis *et al.*, 2013.

example, lasers of $\sim 10^{20}$ W/cm^2 could be expected to generate plasmas in uranium nanowires with $n_e \sim 10^{24}$ cm^{-3} and even remove more than 70 electrons from uranium atoms (Purvis *et al.*, 2013).

Furthermore, interactions of short-pulse, high-intensity relativistic lasers with nanometer-scale targets are actively studied to generate high-energy ions, extreme UV, and coherent radiation (Dollar *et al.*, 2011, 2012; Hoerlein *et al.*, 2011; Jung *et al.*, 2011, 2013; Schnuerer *et al.*, 2011; Kar *et al.*, 2012; Kiefer *et al.*, 2013; Margarone *et al.*, 2012; Ter-Avetisyan *et al.*, 2012; Dromey *et al.*, 2012; Hegelich *et al.*, 2013; Zigler *et al.*, 2013; Kondo, Imai, and Nagamiya, 2015). Particular interest has been toward the acceleration of proton and ion beams using novel acceleration mechanisms such as the radiation pressure acceleration and break-out burnafter among others. A few selected examples from these works are highlighted later.

Submicrometer water spray droplets were utilized to produce proton bursts with a narrow spectrum using high-intensity ($\sim 5 \times 10^{19}$ W/cm^2), high-contrast ($\sim 10^{10}$), ultrashort (40 fs) laser pulses (Ter-Avetisyan *et al.*, 2012). Transparent nanotargets (Hegelich *et al.*, 2013) were employed to achieve carbon ion energies in excess of 0.5 GeV with 50–250-nm-thick targets. The peak intensity in these experiments was $(2–6) \times 10^{20}$ W/cm^2.

Comparative effects of femtosecond laser-driven proton acceleration using sub-100-nm-thick diamondlike carbon (DLC) and several micrometer thick Ti target foils have been reported (Schnuerer *et al.*, 2011). A circularly polarized laser beam of intensity $\sim 3 \times 10^{19}$ W/cm^2 and 45 fs pulse duration was used. The results of this work show quite different scalings of the proton energy as a function of laser intensity, energy, and target thickness, which makes it particularly interesting for the design of future experiments.

Recently, acceleration of highly charged Fe ions up to 0.9 GeV using 200 TW femtosecond high-intensity laser was demonstrated (Kondo, Imai, and Nagamiya, 2015). The experiments were carried out on the J-KAREN laser facility with an intensity of $\sim 10^{21}$ W/cm^2 with a pulse duration of 35 fs. Targets consisting of 5-nm-thick Fe patches almost uniformly distributed over the 800-nm-thick Al foil were used.

Another aspect of applications of nm scale targets is the generation of EUV and coherent radiation. Dense relativistic electron mirrors have been generated from the interaction of a high-intensity Astra-Gemini pulse laser (6×10^{20} W/cm^2) copropagating with a weaker laser pulse ($\sim 10^{15}$ W/cm^2) with 10-nm-thick DLC and 50-nm-thick carbon freestanding foils (Kiefer *et al.*, 2013). The mirrors shifted the frequency of a counterpropagating laser pulse coherently from the infrared to the EUV. The electron mirror which can move with a speed close to the speed of light and reflects incident light is a viable contribution toward producing high-intensity, high-energy pulses of electromagnetic radiation, potentially bright x-ray pulses according to Einstein's theory of special relativity (Kiefer *et al.*, 2013).

Coherent synchrotron emission has been discovered from electron bunches produced by the Trident laser ($\sim 4 \times 10^{20}$ W/cm^2) and nanometer-scale DLC targets (Dromey *et al.*, 2012). When the target thickness increased from 125 to 200 nm, the harmonic signal level also rose by an average factor of 5. This work promises bright attosecond x-ray pulses using nm scale solid targets.

Therefore, nanostructured solid targets open new research directions that may lead to the extensive studies of *relativistic nanoplasma states*. Importantly, nanostructures play a pivotal role in these processes by enabling highly focused, high-contrast interactions of intense laser beams with matter. These nanostructures are promising to improve coupling of intense laser radiation into the target and may facilitate the development of more efficient next-generation sources of extreme radiation and high-energy particles for applications in particle accelerators, medical radiography, materials microanalysis, and several others. These possibilities are awaiting practical realization and offer excellent opportunities for multidisciplinary research and development.

X. CONCLUSION AND OUTLOOK

Localizing plasmas, the fourth and the most extreme state of matter to the nanoscale dimensions, leads to the many interesting and unusual physical effects and is promising for a range of advanced applications. On the other hand, it is difficult to achieve nanoplasmas and measure their properties, compared to the other three states of matter. Because of the number of basic criteria related to the plasma confinement, coupling, ideality, and degeneracy to be satisfied, the known nanoplasma states are transient, highly nonequilibrium, and feature very high electron densities.

Localization of such high densities of ionized matter to nanometer domains may create very high levels of energy densities, even in relatively simple and inexpensive tabletop experiments. The arising high-energy density leads to the many interesting and unusual effects. A viable possibility to achieve the previously elusive nanoplasma states is through the interaction of electromagnetic radiation with varied frequency and intensity with solid matter. This has become possible only fairly recently with the advent of high-intensity femtosecond pulsed lasers and related diagnostic techniques and has sparked intense interdisciplinary research efforts.

We have discussed how the responses of solid matter vary from very low to very high intensities of radiation. At low radiation intensities, plasmalike electronic responses (studied in plasmonics) arise, without plasma generation. Nanoplasmas may arise in solids with photoexcited electrons and holes localized to quantum wells; the plasma density can be controlled by the laser intensity. At higher intensities, escalated nonequilibrium conditions may lead to warm-dense-matter-based nanoplasma states. Nanoplasma generation and related effects are discussed under conditions of laser-induced microexplosions, ionization of nanoclusters and nanostructured targets, and some other cases.

Such localized high-energy-density plasmas may be useful for fundamental studies of matter under extreme conditions (Rosner *et al.*, 2009), in particular, in relation to ultrafast excitation of nanosystems where the transferred energy should be localized at a given site (Stockman, Faleev, and Bergman, 2002). Study of nanoplasma dynamics is thus of interest to both nanoscale physics and physics of ultrafast phenomena because of the characteristic spatial localization scales and transient, nonequilibrium, ultrafast dynamics, which can be achieved by concentration of relatively low energy in very small volumes potentially leading to extreme energy densities. For example, concentrating a small $\sim 10^{-13}$ J into a volume of ~ 1000 nm^3 over 100 fs may lead to the large power density of $\sim 10^{24}$ W/m^3. Under such conditions, plasma is likely to be the only possible state, and reliable approaches to study and control it are required.

Nanoplasma research encompasses elements of both high-energy-density and nanoscale science. Plasma-aided nanofabrication (Ostrikov, 2005) can be used to prepare nanostructured materials with the properties tailored for the interactions with intense radiation. Research at the cross roads of these fields may lead to many unexpected discoveries and practical applications in the future.

We have discussed a number of potential applications of nanoplasmas in diverse situations where high-energy-density, nonequilibrium states of matter can lead to exotic phenomena that are highly unusual at normal conditions. Some of these applications include particle accelerators, compact synchrotrons, sources of THz, infrared, and x-ray radiation, as well as inertial laser fusion. An interplay of these phenomena with nanoscale localization effects is an unexplored field of research, with many interesting and promising possibilities in the future. Finally, we hope that this Colloquium will stimulate discussions and interest to this mature, yet rapidly expanding multidisciplinary research field.

ACKNOWLEDGMENTS

We sincerely thank many of our colleagues for fruitful collaborations, discussions, and critical comments, as well as all researchers who have contributed to the relevant fields, with apologies for not being able to mention anyone specific due to limited space. This work was partially supported by the Australian Research Council and CSIRO OCE Science Leadership Program.

REFERENCES

Alfvén, H., 1939, Phys. Rev. **55**, 425.
Almand-Hunter, A. E., S. T. Cundiff, M. Mootz, M. Kira, and S. W. Koch, 2014, Nature (London) **506**, 471.
Ao, T., Y. Ping, K. Widman, D. F. Price, E. Lee, H. Tam, P. T. Springer, and A. Ng, 2006, Phys. Rev. Lett. **96**, 055001.
Bader, S. D., 2006, Rev. Mod. Phys. **78**, 1.
Bagchi, S., P. P. Kiran, K. Yang, A. M. Rao, M. K. Bhuyan, M. Krishnamurthy, and G. R. Kumar, 2011, Phys. Plasmas **18**, 014502.
Barth, J. V., G. Costantini, and K. Kern, 2005, Nature (London) **437**, 671.
Beg, F. N., A. R. Bell, A. E. Dangor, C. N. Danson, A. P. Fews, M. E. Glinsky, B. A. Hammel, P. Lee, P. A. Norreys, and M. Tatarakis, 1997, Phys. Plasmas **4**, 447.
Bell, A., J. Davies, S. Guerin, and H. Ruhl, 1997, Plasma Phys. Controlled Fusion **39**, 653.
Blaber, M. G., M. D. Arnold, and M. J. Ford, 2009, J. Phys. Chem. C **113**, 3041.
Bliokh, K. Y., Y. P. Bliokh, V. Freilikher, S. Savel'ev, and F. Nori, 2008, Rev. Mod. Phys. **80**, 1201.
Bostedt, C., *et al.*, 2008, Phys. Rev. Lett. **100**, 133401.
Boulais, E., R. Lachaine, and M. Meunier, 2012, Nano Lett. **12**, 4763.
Buividas, R., G. Gervinskas, A. Tadich, B. C. Cowie, V. Mizekis, A. Vailinois, D. de Ligny, E. G. Gamaly, A. V. Rode, and S. Juodkazis, 2014, Adv. Eng. Mater. **16**, 767.
Castro Neto, A. H., F. Guinea, N. M. R. Peres, K. S. Novoselov, and A. K. Geim, 2009, Rev. Mod. Phys. **81**, 109.
Celliers, P., A. Ng, G. Xu, and A. Forsmann, 1992, Phys. Rev. Lett. **68**, 2305.
Chakravarty, U., A. Arora, J. A. Chakera, P. A. Naik, H. Srivastava, P. Tiwari, A. Srivastava, and P. D. Gupta, 2011, J. Appl. Phys. **109**, 053301.
Charlier, J. C., X. Blase, and S. Roche, 2007, Rev. Mod. Phys. **79**, 677.
Chen, F. F., 1984, *Introduction to Plasma Physics and Controlled Fusion* (Plenum Press, New York).
Chen, Z., B. Holst, S. E. Kirkwood, V. Sametoglu, M. Reid, Y. Y. Tsui, V. Recoules, and A. Ng, 2013, Phys. Rev. Lett. **110**, 135001.
Cho, B. I., *et al.*, 2011, Phys. Rev. Lett. **106**, 167601.
Cristoforetti, G., *et al.*, 2014, Plasma Phys. Controlled Fusion **56**, 095001.
D'Angola, A., E. Boella, and G. Coppa, 2014, Phys. Plasmas **21**, 082116.
Daraszewicz, A. L., Y. Giret, N. Naruse, Y. Mureooka, J. Yang, D. M. Duffy, A. L. Shluger, and K. Tanimura, 2013, Phys. Rev. B **88**, 184101.
Debye, P., 1913, Ann. Phys. (Berlin) **348**, 49.
Ditmire, T., T. Donnelly, A. M. Rubenchik, R. W. Falcone, and D. M. Perry, 1996, Phys. Rev. A **53**, 3379.

Ditmire, T., J. Zweiback, Y. P. Yanovsky, T. E. Cowan, G. Hays, and K. B. Wharton, 1999, Nature (London) **398**, 489.
Dobrynin, A. V., R. H. Colby, and M. Rubinstein, 1995, Macromolecules **28**, 1859.
Dollar, F., *et al.*, 2011, Phys. Rev. Lett. **107**, 065003.
Dollar, F., *et al.*, 2012, Phys. Rev. Lett. **108**, 175005.
Dromey, B., *et al.*, 2012, Nat. Phys. **8**, 804.
Dumitrica, T., and R. E. Allen, 2002, Phys. Rev. B **66**, 081202(R).
Dvornikov, M., 2011, Proc. R. Soc. A **468**, 415.
Ernstorfer, R., M. Harb, C. T. Hebeisen, G. Sciani, T. Dartigalongue, and R. J. D. Miller, 2009, Science **323**, 1033.
EUV lithography, 2015, Cymer, http://www.cymer.com/euv.
Faenov, A. Ya., A. V. Lankin, I. V. Morozov, G. E. Norman, S. A. Pikuz, and I. Yu. Skobelev, 2009, in *Laser-driven relativistic plasmas applied to science, industry and medicine*, edited by P. R. Bolton, S. V. Bulanov, and H. Daido (AIP, New York), Vol. 77, p. 331.
Fann, W. S., R. Storz, H. W. K. Tom, and J. Bokor, 1992, Phys. Rev. B **46**, 13592.
Feibelman, P. J., 1982, Prog. Surf. Sci. **12**, 287.
Forslund, D. W., J. M. Kindle, and K. Lee, 1977, Phys. Rev. Lett. **39**, 284.
Forsman, A., A. Ng, G. Chiu, and R. M. More, 1998, Phys. Rev. E **58**, R1248.
Fortov, V. E., 2011, *Extreme States of Matter on Earth and in the Cosmos* (Springer, Berlin).
Fortov, V. E., and I. T. Iakubov, 2000, *The Physics of Non-Ideal Plasmas* (World Scientific, Singapore).
Gamaly, E. G., L. Rapp, V. Roppo, S. Juodkazis, and A. V. Rode, 2013, New J. Phys. **15**, 025018.
Gamaly, E. G., A. V. Rode, B. Luther-Davies, and V. T. Tikhonchuk, 2002, Phys. Plasmas **9**, 949.
Gamaly, E. G., A. Vailionis, V. Mizeikis, W. Yang, A. V. Rode, and S. Juodkazis, 2012, High Energy Density Phys. **8**, 13.
Glenzer, S. H., *et al.*, 2007, Phys. Rev. Lett. **98**, 065002.
Glenzer, S. H., *et al.*, 2012, Phys. Plasmas **19**, 056318.
Gonze, X., *et al.*, 2002, Comput. Mater. Sci. **25**, 478.
Grigoryan, N. S., E. S. Zijlstra, and M. E. Garcia, 2014, New J. Phys. **16**, 013002.
Hao, E., and G. C. Schatz, 2004, J. Chem. Phys. **120**, 357.
Hegelich, B. M., *et al.*, 2013, New J. Phys. **15**, 085015.
Hickstein, D. D., *et al.*, 2014, Phys. Rev. Lett. **112**, 115004.
Hillyard, H. O., D. A. Reis, and K. J. Gaffney, 2008, Phys. Rev. B **77**, 195213.
Hoerlein, R., *et al.*, 2011, Laser Part. Beams **29**, 383.
Hohlfeld, J., J. G. Muller, S.-S. Wellershoff, and E. Matthias, 1997, Appl. Phys. B **64**, 387.
Hohlfeld, J., S.-S. Wellershoff, J. Gudde, U. Conrad, V. Jahnke, and E. Matthias, 2000, Chem. Phys. **251**, 237.
Holst, B., V. Recoules, S. Mazevet, M. Torrent, A. Ng, Z. Chen, S. E. Kirkwood, V. Sametoglu, M. Reid, and Y. Y. Tsui, 2014, Phys. Rev. B **90**, 035121.
Hoyaux, M. F., 1968, Contemp. Phys. **9**, 165.
Huber, R., F. Tauser, A. Brodschelm, M. Bichler, and A. Leitenstorfer, 2001, Nature (London) **414**, 286.
Ichimaru, S., 1982, Rev. Mod. Phys. **54**, 1017.
Jeffries, C., 1975, Science **189**, 955.
Jeschke, H. O., M. E. Garcia, and J. A. Alonso, 2002, Chem. Phys. Lett. **352**, 154.
Jeschke, H. O., M. E. Garcia, and K. H. Bennemann, 1999, Phys. Rev. B **60**, R3701.
Jeschke, H. O., M. E. Garcia, and K. H. Bennemann, 2001, Phys. Rev. Lett. **87**, 015003.
Jonscher, A. K., 1964, Br. J. Appl. Phys. **15**, 365.
Jung, D., *et al.*, 2011, Phys. Rev. Lett. **107**, 115002.
Jung, D., *et al.*, 2013, New J. Phys. **15**, 023007.
Juodkazis, S., H. Misawa, O. A. Louchev, and K. Kitamura, 2006, Nanotechnology **17**, 4802.
Kabashin, A. V., Ph. Delaporte, A. Pereira, D. Grojo, R. Torres, Th. Sarnet, and M. Sentis, 2010, Nanoscale Res. Lett. **5**, 454.
Kabeer, F. C., E. S. Zijlstra, and M. E. Garcia, 2014, Phys. Rev. B **89**, 100301.
Kahaly, S., S. K. Yadav, W. M. Wang, S. Sengupta, Z. M. Sheng, A. Das, P. K. Kaw, and G. R. Kumar, 2008, Phys. Rev. Lett. **101**, 145001.
Kaindl, R. A., M. A. Carnahan, D. Haegele, R. Loevenich, and D. S. Chemla, 2003, Nature (London) **423**, 734.
Kar, S., *et al.*, 2012, Phys. Rev. Lett. **109**, 185006.
Keldysh, L. V., 1986, Contemp. Phys. **27**, 395.
Kiefer, D., *et al.*, 2013, Nat. Commun. **4**, 1763.
Koenig, M., *et al.*, 2005, Plasma Phys. Controlled Fusion **47**, B441.
Kohn, J., R. Redmer, and T. Fennel, 2012, New J. Phys. **14**, 055011.
Kondo, K., K. Imai, and S. Nagamiya, 2015, Phys. Plasmas **22**, 033107.
Krishnan, S. R., *et al.*, 2011, Phys. Rev. Lett. **107**, 173402.
Lapine, M., I. V. Shadrivov, and Y. S. Kivshar, 2014, Rev. Mod. Phys. **86**, 1093.
Lee, R. W., *et al.*, 2003, J. Opt. Soc. Am. B **20**, 770.
Lin, Z., L. V. Zhigilei, and V. Celli, 2008, Phys. Rev. B **77**, 075133.
Lower, Th., V. N. Kondrashov, M. Basko, A. Kendl, J. Meyer-ter-Vehn, R. Sigel, and A. Ng, 1998, Phys. Rev. Lett. **80**, 4000.
Maier, S., and H. Atwater, 2005, J. Appl. Phys. **98**, 011101.
Margarone, D., *et al.*, 2012, Phys. Rev. Lett. **109**, 234801.
Marklund, M., and P. K. Shukla, 2006, Rev. Mod. Phys. **78**, 591.
Mazevet, S., J. Clerouin, V. Recoules, P. M. Anglade, and G. Zerah, 2005, Phys. Rev. Lett. **95**, 085002.
Micheau, S., H. Jouin, and B. Pons, 2008, Phys. Rev. A **77**, 053201.
Mikaberidze, A., U. Saalmann, and J. M. Rost, 2009, Phys. Rev. Lett. **102**, 128102.
Morfill, G., and A. Ivlev, 2009, Rev. Mod. Phys. **81**, 1353.
Mulvaney, P., J. Perez-Juste, M. Giersig, L. M. Liz-Marzan, and C. Pecharroman, 2006, Plasmonics **1**, 61.
Neumayer, P., *et al.*, 2010, Phys. Rev. Lett. **105**, 075003.
Ng, A., Int. J. Quantum Chem. 2012, **112**, 150.
Ng, A., T. Ao, F. Perrot, M. W. C. Dharma-Wardana, and M. E. Foord, 2005, Laser Part. Beams **23**, 527.
Nouvel, P., *et al.*, 2009, J. Appl. Phys. **106**, 013717.
Ostrikov, K., 2005, Rev. Mod. Phys. **77**, 489.
Ostrikov, K. N., S. Xu, and S. Lee, 2000, Phys. Scr. **62**, 189.
Paul, T., C. Rockstuhl, and F. Lederer, 2011, J. Mod. Opt. **58**, 438.
Pines, D., 1956, Rev. Mod. Phys. **28**, 184.
Ping, Y., D. Hanson, I. Koslow, T. Ogitsu, D. Prendergast, E. Schwegler, G. Collins, and A. Ng, 2006, Phys. Rev. Lett. **96**, 255003.
Purvis, M. A., *et al.*, 2013, Nat. Photonics **7**, 796.
Raimes, M. F., 1957, Rep. Prog. Phys. **20**, 1.
Recoules, V., G. Clerouin, A. Zerah, P. M. Anglade, and S. Mazevet, 2006, Phys. Rev. Lett. **96**, 055503.
Rosmej, O. N., *et al.*, 2005, Phys. Rev. A **72**, 052901.
Rosner, R., *et al.*, 2009, "Basic research needs for high energy density laboratory physics, U.S. Department of Energy, Washington DC," http://nnsa.energy.gov/sites/default/files/nnsa/01-13-inlinefiles/Basic%20Research%20Needs%20in%20HEDLP-ReNeW-Download-opt_2011.pdf.
Rousse, A., *et al.*, 2001, Nature (London) **410**, 65.
Rozet, J. P., *et al.*, 2001, Phys. Scr. **T92**, 113.

Schnuerer, M., *et al.*, 2011, Laser Part. Beams **29**, 437.
Shalaev, V. M., 2007, Nat. Photonics **1**, 41.
Siders, C. V., A. Cavalleri, K. Sokolowski-Tinten, C. Toth, T. Guo, M. Kammler, M. Horn von Hoegen, K. R. Wilson, D. von der Linde, and C. P. J. Barty, 1999, Science **286**, 1340.
Silverinha, M. G., 2009, Phys. Rev. B **79**, 035118.
Silvestrelli, P. L., A. Alavi, M. Parrinello, and D. Frenkel, 1996, Phys. Rev. Lett. **77**, 3149.
Silvestrelli, P. L., and M. Parrinello, 1998, J. Appl. Phys. **83**, 2478.
Singh, P. K., *et al.*, 2012, Appl. Phys. Lett. **100**, 244104.
Singh, P. K., *et al.*, 2013, Phys. Rev. ST Accel. Beams **16**, 063401.
Sivis, M., and C. Ropers, 2013, Phys. Rev. Lett. **111**, 085001.
Smith, R. P., *et al.*, 2010, Phys. Rev. Lett. **104**, 247401.
Sokolowski-Tinten, K., C. Blome, A. Dietrich, A. Tarasevich, D. Horn von Hoegen, D. von der Linde, A. Cavallerim, J. Squier, and M. Kammler, 2001, Phys. Rev. Lett. **87**, 225701.
Stampfli, P., and K. H. Bennemann, 1990, Phys. Rev. B **42**, 7163.
Stampfli, P., and K. H. Bennemann, 1992, Phys. Rev. B **46**, 10686.
Stockman, M. I., 2011, Phys. Today **64**, 39.
Stockman, M. I., S. V. Faleev, and D. J. Bergman, 2001, Phys. Rev. Lett. **87**, 167401.
Stockman, M. I., S. V. Faleev, and D. J. Bergman, 2002, Phys. Rev. Lett. **88**, 067402.
Sun, Q., K. Ueno, H. Yu, A. Kubo, Y. Matsuo, and H. Misawa, 2013, Light Sci. Appl. **2**, e118.
Suzuki, T., and R. Shimano, 2009, Phys. Rev. Lett. **103**, 057401.
Ter-Avetisyan, S., *et al.*, 2012, Phys. Plasmas **19**, 073112.
Townsend, E., and G. W. Bryant, 2012, Nano Lett. **12**, 429.
Vailinois, A., E. G. Gamaly, V. Mizekis, W. Yang, A. V. Rode, and S. Juodkazis, 2011, Nat. Commun. **2**, 445.
Varin, C., C. Peltz, T. Brabec, and T. Fennel, 2012, Phys. Rev. Lett. **108**, 175007.
Wabnitz, H., *et al.*, 2002, Nature (London) **420**, 482.
Waller, I., 1923, Z. Phys. **17**, 398.
Wang, X. D., J. H. Song, J. Liu, and Z. L. Wang, 2007, Science **316**, 102.
Wang, Y., E. W. Plummer, and K. Kempa, 2011, Adv. Phys. **60**, 799.
Widmann, K., T. Ao, M. E. Foord, D. F. Price, A. D. Ellis, P. T. Springer, and A. Ng, 2004, Phys. Rev. Lett. **92**, 125002.
Wiley, B. J., Y. Chen, J. M. McLellan, Y. Xiong, Z. Y. Li, D. Ginger, and Y. Xia, 2007, Nano Lett. **7**, 1032.
Willets, K. A., and R. P. van Duyne, 2007, Annu. Rev. Phys. Chem. **58**, 267.
Willmott, P., and J. Huber, 2000, Rev. Mod. Phys. **72**, 315.
Zayats, A. V., I. Smolyaninov, and A. A. Maradudin, 2005, Phys. Rep. **408**, 131.
Zigler, A., *et al.*, 2013, Phys. Rev. Lett. **110**, 215004.
Zijlstra, E. S., A. Kalitsov, T. Zier, and M. E. Garcia, 2013, Adv. Mater. **25**, 5605.